NPL Report CMMT(A)266

June 2000

Illustrations of the Application of Finite Element and Processing Simulation Analyses to Plastics

G Dean*, R Hunt* and R Shastri†
Centre for Materials Measurement and Technology and
National Physical Laboratory,
Teddington, Middlesex TW11 0LW

SUMMARY

This report contains the Annexes to the ISO standard Guide ISO 17282 that is currently under development and is concerned with test methods and analyses for determining design data for plastics. The design data are required by design procedures that are based on computer analyses that are available for predicting the performance of a component in service or for simulating its manufacture by various processing methods.

The Annexes to the ISO Guide are reproduced here and illustrate the acquisition and use of the data needed for different types of analysis. For finite element analyses, the application of different materials models is illustrated for describing the behaviour of plastics under circumstances where behaviour is elastic, rate-, time- or frequency-dependent, non-linear or anisotropic. The processing methods covered are injection moulding, extrusion, blow moulding, blown-film extrusion and thermoforming.

These Annexes are not yet complete and further parts will be added before the development of the Guide is complete in ISO TC61.

* Centre for Materials Measurement and Technology, National Physical Laboratory, Teddington, Middlesex TW11 0LW
† Dow Chemical Company, Materials Engineering Center, 433 Building Midland, MI 48667, USA

© Crown copyright 2000
Reproduced by permission of the Controller of HMSO

ISSN 1361-4061

National Physical Laboratory
Teddington, Middlesex, UK, TW11 0LW

Extracts from this report may be reproduced provided the source is acknowledged and the extract is not taken out of context.

Approved on behalf of Managing Director, NPL, by Dr C Lea,
Head, Centre for Materials Measurement and Technology

CONTENTS

SUMMARY 1

ANNEX A1 ILLUSTRATIONS OF THE APPLICATIONS OF FINITE ELEMENT ANALYSES TO PLASTICS 1

A1 COMPONENT GEOMETRY AND LOADING ARRANGEMENT 2
A2 APPLICATION OF A LINEAR ELASTIC MATERIALS MODEL 2
A3 APPLICATION OF A NON-LINEAR ELASTIC MATERIALS MODEL 3
A4 APPLICATION OF ELASTIC-PLASTIC MODELS 4
A4.1 Derivation of materials parameters 6
A4.2 Comparison of FE analyses 8
A4.3 Summary of section A4 8
A5 APPLICATION OF AN ELASTIC-PLASTIC MODEL WITH STRAIN-RATE DEPENDENT MATERIALS PROPERTIES 9
A6 APPLICATION OF A NON-LINEAR CREEP MODEL 9
A7 APPLICATION OF A LINEAR VISCOELASTIC MATERIALS MODEL 15
A8 APPLICATION OF AN ANISOTROPIC ELASTIC MODEL 17

ANNEX B APPLICATION OF PROCESSING SIMULATION ANALYSIS FOR PLASTICS 19

B1 SIMULATION OF THE INJECTION MOULDING PROCESS 23
B1.1 Illustration of simple mould filling analysis of thermoplastics 23
B1.2 Illustration of advanced mould filling, packing and cooling analysis of thermoplastics 25
B1.3 Illustration of shrinkage/warpage analysis 28
B2 SIMULATION OF THE EXTRUSION PROCESS 29
B2.1 Illustration of analysis of polymer melting in the extruder 30
B2.2 Illustration of the analysis of sheet extrusion process – polymer melt flow in a coat hanger die 31
B2.3 Illustration of the analysis of profile extrusion process – polymer melt flow in a profile die 31
B3 SIMULATION OF BLOW MOLDING PROCESS 32
B4 SIMULATION OF BLOWN FILM EXTRUSION PROCESS 32

ANNEX A

ILLUSTRATIONS OF THE APPLICATIONS OF FINITE ELEMENT ANALYSES TO PLASTICS

In this annex, the application of finite element methods is illustrated by calculations of stress and strain distributions in plastics subjected to different loading situations. A range of types of material behaviour is considered. The aim is to show how the parameters required by various materials models used in FE analysis can be derived from experimental data. Descriptions here are necessarily brief and reference should be made to technical literature and FEA user manuals for more detailed information.

The applications considered are shown in table A1.

Table A1. Applications of finite element analyses considered in this section

Section	Behaviour	Loading	Model type
A2	Linear elastic	Static	A
A3	Non-linear elastic	Static	B
A4	Non-linear (elastic plastic)	Static	C
A5	Non-linear (rate-dependent plasticity)	Impact	C3
A6	Non-linear viscoelastic	Creep	E1 or (C1)
A7	Linear viscoelastic	Dynamic	D2
A8	Anisotropic linear elastic	Static	A

A1 COMPONENT GEOMETRY AND LOADING ARRANGEMENT

In sections A2 to A6, the application of different materials models is considered to a single component geometry and loading arrangement. The component is a circular plate that is simply supported on a ring close to its circumference and loaded at its centre as shown in figure 1. The selected dimensions correspond closely with those used for puncture impact tests described in ISO 6603-2. Note that a specimen thickness of 3 mm has been chosen in place of the 2 mm thickness recommended in the ISO standard. The element mesh for the specimen is shown in figure 2 where it can be seen that the loading device and the support are defined by a linear mesh which assumes that these parts are infinitely rigid compared with the plate.

A2 APPLICATION OF A LINEAR ELASTIC MATERIALS MODEL

With this model, stress and strain components are considered to be linearly related at all levels of strain. However, geometric non-linearity, which allows for changes in the geometry of the plate brought about by large central displacements, is taken into account in the analysis. According to table 2a, the data requirements for this model are the tensile modulus E and the Poissons ratio ν. As indicated in Table 6, these can be determined from a tensile test following the procedure described in ISO 527. Any dependence of properties on the rate of loading or the time under load is not taken into consideration in the analysis but associated errors can be minimised by using data measured at strain rates or loading times appropriate to the application.

Results from a tensile test on a propylene copolymer are shown in figure 3 measured at a constant deformation rate of 10 mm/min. This corresponds to an elastic strain rate of $2\ 10^{-3}\ s^{-1}$. Values for the tensile modulus of 1.6 GPa and for Poisson's ratio of 0.39 are obtained from the data in the strain range up to 0.01 which marks the limit of linear behaviour. Using these values, a finite element analysis has been used to obtain the variation of the force applied by the hemispherical contact with the central deflection of the plate. This is shown in figure 4 where it is compared with results derived from a non-linear analysis (see section A4). Figure 5 shows the distribution of the tensile component of strain in the radial direction at a central deflection of 4 mm. In certain regions of the plate, the strain magnitude is above the limit for linear

behaviour and this is consistent with the observed departure of the predicted curve in figure 4 from the curve based on a model for non-linear behaviour.

A3 APPLICATION OF A NON-LINEAR ELASTIC MATERIALS MODEL

Errors in the linear elastic analysis become progressively more significant at deflections where strain levels in the plate exceed the limit for linear behaviour. More accuracy in predictions can then be achieved using a hypoelastic model that allows for some non-linearity in the stress/strain curve in figure 3. The data requirements for this model are shown in table A2.

Table A2. Data requirements for a hypoelastic model derived from the data on the propylene copolymer shown in figure 3

ε	E_T	ν_T	I_1	I_2	I_3
-.06	0.075	0.459	-1.570E-02	2.168E-03	-2.944E-05
-.04	0.252	0.457	-6.032E-03	1.070E-03	-1.154E-05
-.02	0.818	0.455	-2.768E-03	2.704E-04	-1.485E-06
-.01	1.200	0.433	-1.754E-03	6.546E-05	-1.700E-07
0	1.600	0.390	0.000E+00	0.000E+00	0.000E+00
.01	1.200	0.433	1.754E-03	6.546E-05	1.700E-07
.02	0.818	0.455	2.768E-03	2.704E-04	1.485E-06
.04	0.252	0.327	6.032E-03	1.070E-03	1.154E-05
.06	0.075	0.221	1.570E-02	2.168E-03	2.944E-05
.08	0.013	0.176	2.880E-02	3.441E-03	5.243E-05
.1	0.003	0.157	4.216E-02	4.948E-03	8.364E-05
.2	0.001	0.122	1.163E-01	1.499E-02	3.501E-04

E_T are values for the tangent tensile modulus obtained as a function of tensile strain ε and are equal to the gradient of the stress/strain curve at the strain ε. ν_T are values for the tangent Poisson's ratio and are equal to the gradient of the plot of lateral strain against longitudinal strain at the strain ε. I_1, I_2 and I_3 are strain invariants and are related to the tensile strain ε as follows:

$$I_1 = (1-2\nu)\varepsilon$$
$$I_2 = \nu\varepsilon^2(2-\nu) \qquad \text{(A1)}$$
$$I_3 = \nu^2\varepsilon^3$$

At values of I_1, I_2 and I_3 where ε lies in the linear region of strain, E_T and ν_T are the linear elastic values E and ν_e. The force/deflection curve shown in figure 6 is predicted using this model. Figure 7 shows contours of the tensile component of strain at a central deflection of 4 mm.

A4 APPLICATION OF ELASTIC-PLASTIC MODELS

The limitations in the accuracy achievable with the hypoelastic model are not well understood but it seems that the model is unreliable under conditions of high strain and multiaxial stress. Elastic-plastic models are potentially more accurate under these conditions although it should be noted that they have been developed to describe deformation in metallic and certain other materials and their applicability to plastics is still a subject for further research. Non-linearity in a stress/strain curve is interpreted as due to plastic deformation, and the stress that marks the onset of curvature is considered as the first yield point. (Contrast this with the terminology used for plastics materials where non-linear deformation is largely recoverable and the yield point is the peak stress in the stress/ strain curve.) The subsequent increase of stress with strain is interpreted as strain hardening. In this region of strain, the total strain is considered to be comprised of both elastic and plastic components, the latter, according to the model, being non-recoverable. For this reason, elastic-plastic models would not be expected to apply to plastics in situations involving any reversal of the load.

In order to describe the contribution from plasticity to the total deformation, a knowledge is needed of parameters that characterise yielding and plastic strain hardening of the material. The yield parameters are defined by the yield criterion for the material and the strain hardening behaviour is determined by the shape of the tensile stress/strain curve.

With metals, yielding is commonly assumed to be dependent only upon the shear component of the applied stress. In this case the yield criterion is given by the von Mises equation

$$\sigma_T = \sqrt{3}\ J_{2D}^{1/2}$$

where J_{2D} is an effective shear stress and is a function of the components of the applied stress. In terms of components of principal stress σ_1, σ_2, σ_3

$$J_{2D} = \frac{1}{6}\left[(\sigma_1-\sigma_2)^2 + (\sigma_2-\sigma_3)^2 + (\sigma_3-\sigma_1)^2\right]$$

In equation (A2), σ_T is a yield stress in uniaxial tension and, for a strain hardening material, will increase with the plastic component of strain. Methods for determining σ_T and its dependence on plastic strain are explained in the next sub-section.

The von Mises yield criterion adequately describes the yield behaviour of only a limited number of plastics materials. In general, yielding is sensitive to both the shear and the hydrostatic components of stress and a modification to equation (A2) is more appropriate. The simplest modification considers the yield stress to be linearly related to the hydrostatic stress component J_1 so that equation (A2) becomes

$$\sigma_T = \frac{\sqrt{3}(\lambda+1)}{2\lambda}\ J_{2D}^{1/2} + \frac{(\lambda-1)}{2\lambda}\ J_1$$

where

$$J_1 = \sigma_1 + \sigma_2 + \sigma_3$$

The parameter λ is a measure of the sensitivity of yield behaviour to the hydrostatic component of stress. When $\lambda = 1$, equation (A4) reduces to equation (A2).

Equation (A4) is identical to the linear Drucker-Prager model used is several FE packages and developed to describe slip in soil and related materials. Other models, with different forms for the hydrostatic stress sensitivity, are the Mohr-Coulomb and the exponent Drucker Prager models.

A4.1 Derivation of materials parameters

The data requirements for elastic-plastic materials models (type C) are listed in table 2a and explained briefly in notes 4, 5 and 6.

Values for the Youngs modulus E and the Poissons ratio ν_e at small strains are generally used to characterise elastic behaviour and to determine elastic components of strain. The shear modulus could be used in place of Poissons ratio for this purpose but Poissons ratio is recorded here because it can be measured in the tests used to determine E (see table 6) and, if lateral strain measurements are extended into the non-linear region, these enable true stresses to be calculated from measured (engineering) values.

The finite element analysis requires data on the dependence of the true tensile yield stress against the true plastic strain. The determination of this function is illustrated in figures 3 and 8. Figure 3 shows a measured tensile stress/strain curve (referred to as the engineering stress) and the associated variation of Poissons ratio with strain. In an elastic-plastic model, the limit of linear behaviour marks the onset of plastic deformation and hence the first yield stress. All stresses on the curve above this are engineering tensile yield stresses σ_Y. If the value of σ_Y corresponds to the strain ε at which the Poissons ratio is ν, then the true tensile yield stress at ε is given by

$$\sigma_T = \frac{\sigma_Y}{(1-\nu\varepsilon)^2}$$

This function is also plotted in figure 3.

Equation (A6) shows that true stress values should generally be used when strains exceed about 0.1.

In an elastic-plastic model, the strains ε corresponding to the non-linear region of figure considered to be the sum of elastic and plastic components. For arbitrary strain levels, these components must be true strains, so the true plastic strain $\log_e(1+\varepsilon_p)$ is given by

$$\log_e(1+\varepsilon_p) = \log_e(1+\varepsilon) - \frac{\sigma_T}{E}$$

where σ_T is the true yield stress at the engineering tensile strain ε. It can be seen that the use of true rather than engineering strains is generally necessary at strains above about 0.1

Figure 8 shows a plot of the true yield stress against the true plastic strain derived from the data in figure 3.

The remaining parameters in table 2a for this model are λ, ν_p and ψ. If the von Mises yield criterion is assumed to be valid then these parameters take values

$$\lambda = 1$$
$$\nu_p = 0.5$$
$$\psi = 0$$

and therefore do not need to be measured. The von Mises yield criterion is likely to be valid for those materials for which Poissons ratio approaches a value of 0.5 with increasing tensile strain. Many plastics, especially multiphase systems, however show a decrease in Poissons ratio with strain which is probably associated with a plastic deformation mechanism that involves crazing or cavitation. The onset of this yield mechanism is indicated by a reduction in Poissons ratio as shown in figure 3. The yielding of these materials is better described by a pressure sensitive criterion such as that given in equation (A4). Procedures have been reported for determining λ from additional tests under a different stress state such as shear or compression.

An estimate for the flow parameter ψ can be obtained from measurements of the plastic component of Poissons ratio ν_p (see figure 8) using the equation

$$\tan\psi = \frac{3(1-2\nu_p)}{2(1+\nu_p)}$$

where ν_p is calculated from measurements of the lateral strain ε_t and is given by

$$\nu_p = -\left[\frac{\log_e(1+\varepsilon_t)+\frac{\nu_e\sigma_T}{E}}{\log_e(1+\varepsilon_p)}\right] \qquad \text{(A9)}$$

Comparison of FE analyses

Figures 9 and 10 show calculations of the force-deflection curve and strain distributions for the centrally loaded plate. Two materials models have been used. One is based on the von Mises criterion (equation (A2)) where the required materials parameters are the Youngs modulus, the elastic component of Poisson's ratio and the strain hardening function σ_T (ε_p) derived from the data shown in figures 3 and 8. The other model has employed a hydrostatic stress sensitive yield criterion (equation (A4)) with the same tensile data as used in the von Mises model but with a value for λ = .5 and for $\psi = 30^o$. It can be seen that the strain patterns and the force/deflection curves are similar but the maximum strain levels predicted by each model are significantly different.

A4.3 Summary of section A4

A stress/strain curve in tension is the basic data requirement for an elastic-plastic analysis. From these data, a plot of tensile yield stress against plastic strain is derived. If this is the only material property information available, then a realistic value for Poissons ratio at small strains must be estimated and von Mises yielding must be assumed.

If measurements of Poissons ratio are also available to large strains, then true tensile yield stress values can be calculated. These values are only needed if strains exceeding about 0.1 are generated. In these situations, true plastic strain values should also be used.

A stress/strain curve under an alternative stress state, such as compression or shear, is required to explore the need to use a yield criterion that is sensitive to the hydrostatic component of stress. Such yield criteria are employed in the Drucker-Prager and Mohr-Coulomb materials models. A hydrostatic stress sensitivity parameter for these models can be derived from the two stress/strain curves.

In the application considered here, the force-deflection curve calculated using a realistic yield criterion was similar to that obtained using the von Mises approximation. Values for the maximum strain in the plate were however significantly different. This difference might be important if the analysis were used in conjunction with a failure criterion based on a critical level of strain.

A5 APPLICATION OF AN ELASTIC-PLASTIC MODEL WITH STRAIN-RATE DEPENDENT MATERIALS PROPERTIES

The deformation behaviour of plastics is sensitive to the rate of loading. Stress/strain data depend upon the strain rate, and hence cross-head speed, used to obtain the data. Some FE packages will carry out an elastic-plastic analysis with rate dependent materials properties. The input data are then derived from stress/strain curves measured over a range of constant strain rates. Such data are shown in figure 11 for the propylene copolymer. Because waisted specimens are used, the strain rate increases by a factor of about 2 during the tests. The recorded values are plastic strain rates and are larger than the elastic strain rate corresponding to the initial stages of a test. Curves of yield stress against plastic strain ($\sigma_T(\varepsilon_p)$) were derived from these plots at each strain rate. A small variation of the tensile modulus with rate was also observed.

A dynamic analysis was used with these data to predict the force against deflection for the centrally loaded plate in figure 1 when deformed at different speeds. Values for the density of the plate and the impactor are also needed so that inertia contributions can be included. The pressure-sensitive yield criterion employed in section A4 was used with values for λ=1.5 and ψ=30° assumed to be independent of strain rate. An explicit solver code was used for the analysis. Results for a range of loading speeds are shown in figure 12.

A6 APPLICATION OF A NON-LINEAR CREEP MODEL

Creep in plastics is caused by relaxation processes in which time-dependent changes in the conformation of polymer molecules take place in response to an applied stress σ_o.

resulting creep deformation of the material is characterised by a time-dependent strain $\varepsilon(t)$ from which a creep compliance function

$$D(t) = \varepsilon(t) / \sigma_o \qquad \text{(A10)}$$

is derived.

Creep behaviour is most commonly studied using tensile creep experiments in which case $D(t)$, $\varepsilon(t)$ and σ_o are then associated with the tensile compliance, tensile strain and tensile stress respectively. A number of mathematical functions have been used to model experimental results. The function

$$D(t) = D_o \exp(t/\tau)^n \qquad \text{(A11)}$$

has been used successfully for plastics at temperatures well below their glass transition temperature. The parameter τ is identified with a mean retardation time for the creep process which has a distribution of retardation times related to the magnitude of the parameter m. D_o is the elastic compliance and is equal to the inverse of the Young's modulus measured at an appropriate strain rate.

Since the parameter τ in equation (A11) is assumed to be constant, the equation does not take account of physical ageing in the material. Physical ageing is associated with a slow reorganisation of the structure of the polymer following cooling from its processing temperature. These changes reduce the molecular mobility over a long period of time which, under creep loading, gives rise to a progressive increase in the parameter τ with creep time. This produces a shift in the creep function at large creep times which can be modelled if the age and ageing rate of the material are known.

For small creep stresses, τ is independent of the stress magnitude and the creep behaviour is linear. At higher stresses, creep curves are observed to shift to shorter times as shown in figure 13 for experimental data obtained on PVC. This shift is interpreted as an increase in molecular mobility brought about by the application of elevated stresses that results in a

reduction in the mean retardation time τ. It is this enhanced mobility that gives rise to non-linear creep behaviour. The increase in mobility is short lived and, subsequent to load application, τ increases relatively quickly with time under load analagous to enhanced physical ageing. Modelling the stress and time dependences of τ and how they influence the creep deformation is still a subject for further research.

For the application considered here, the effects of physical ageing on the creep compliance will have to be neglected. For this situation, the creep data in figure 13 can be adequately modelled by a simple power law as follows

$$D(t) = D_o (1 + (t/\tau)^n) \qquad \text{(A12)}$$

Values for the parameters D_o, τ and n have been chosen to give the optimum fit to the experimental data. The fits are shown in figure 13. The values for D_o and m are the same for each curve. The parameter τ is different for each stress level but is assumed constant with creep time. This neglect of any variation of τ with creep time is responsible for the inability of equations (A11) or (A12) to accurately describe the shape of the experimental results. The dependence of τ on stress is adequately described by the following relationship which is based on the Eyring equation for molecular transitions across a potential barrier whose height is changed by the applied stress.

$$\tau = \frac{A \sigma_t}{\sinh a \sigma_o} \qquad \text{(A13)}$$

Values for the parameters in equations (A12) and (A13) that were used to obtain the fits to the data in figure 13 are shown in table A3.

Table A3 Values for the parameters in equations (A12) and (A13) used to model creep in PVC

D_o GPa^{-1}	n	A $s.MPa^{-1}$	a MPa^{-1}
0.305	0.28	$4.2.10^6$	0.3

It is worth noting that the values for A and a in table A3, and hence the retardation times τ, depend on the physical age of the material when the load was applied. For the PVC data shown in figure 13, creep stresses were applied 240 hours after specimens had been quenched from the glass transition temperature for PVC. At low stresses (6 MPa and below), the specimen will age significantly during the test, and this has lead to the departure of equation (A12) from creep data. If the specimen had been much older when the creep test were started, then the parameter τ would have been larger but would change less during the test. Equation (A12) would then give a better fit to experimental data as long as the appropriate larger τ value were used. The effect of elevated stresses on the older material would still be to reduce the τ value at load application but τ will increase again subsequently with creep time. This will lead to similar departures of equation (A12) from creep data as illustrated in figure 13.

Equations (A12) and (A13) described creep under a uniaxial tensile stress. However equation (A12) can be generalised to apply to multiaxial creep stress states as follows

$$\varepsilon_{ij}(t) = S_{ijkl}\, \sigma_{kl}\, (1+(t/\tau)^n) \qquad \text{(A14)}$$

$$\tau = \frac{A\bar{\sigma}}{\sinh a\,\bar{\sigma}} \qquad \text{(A15)}$$

The tensor equation (A14) relates components of the time-dependent strain $\varepsilon_{ij}(t)$ to components of applied stress σ_{kl} through the elastic compliance tensor S_{ijkl}. For an isotropic

material, the components of the compliance tensor can be expressed in terms of two material properties, usually the tensile modulus and Poisson's ratio, as shown later in equation (A20).

The parameter $\overline{\sigma}$ is an effective stress and accounts for the observation that the reduction of τ with stress depends on the stress state as well as the stress magnitude. This is demonstrated through an analysis of creep tests under uniaxial compression where the reduction of τ for a given stress level is observed to be significantly less than that obtained under the same uniaxial tensile stress. This suggests that it is the shear component of stress that is mainly responsible for reducing τ, but this reduction is also influenced by the hydrostatic component. By analogy with the influence of hydrostatic stress on yielding in plastics given by equation (A4) in section A4, an expression for $\overline{\sigma}$ of the following form has been considered.

$$\overline{\sigma} = \frac{\sqrt{3}\,(\beta+1)}{2\beta}\, J_{2D}{}^{1/2} + \frac{(\beta-1)}{2\beta}\, J \qquad \text{(A16)}$$

J_1 and $J_{2D}{}^{1/2}$ are invariants of the creep stress matrix and are defined by equations (A3) and (A5) in section A4. From analyses of non-linear creep data for PVC under tension and compression, a value for $\beta = 2$ was derived.

The creep function given by equation (A14) with (A15) treats creep as time-dependent elasticity. Since the time dependent term is also influenced by the stress magnitude, then non-linear behaviour is modelled. Non-linear creep in finite element packages is generally modelled by time-dependent plasticity. These models are widely applicable to creep in metallic materials but require some evaluation before they can be used to represent the behaviour observed with plastics and described by equation (A14).

In time-dependent plasticity models, the total strain is the sum of elastic and plastic components and it is the plastic component that is responsible for time-dependence and hence creep. A general form for the creep strain rate is considered to be the sum of contributions arising from shear and swelling (volumetric) deformation mechanisms. The strain rate of the tensor components of creep strain ε_{ij} is then represented by the equation

$$\dot{\varepsilon}_{ij}(t) = \dot{\varepsilon}_s \left(\frac{\partial q}{\partial \sigma_{ij}} \right) + \dot{\varepsilon}_{sw}\, \delta_{ij} \qquad \text{(A17)}$$

where $\dot{\varepsilon}_s$ and $\dot{\varepsilon}_{sw}$ are the contributions to the strain rate arising from shear and volumetric deformations. The parameter q is used in place of $\sqrt{3}\, J_{2D}^{1/2}$ (see equation (A5)) and is an effective stress and $\delta_{ij} = 1$ for $i = j$ and 0 for $i \neq j$.

It can be shown that

$$\frac{\partial q}{\partial \sigma_{ij}} = \frac{3}{2q}\left(\sigma_{ij} - \sigma_m\, \delta_{ij}\right)$$

where σ_m is the mean stress and is equal to $J_1/3$ (see equation (A3)). Equation (A17) can therefore be written as

$$\dot{\varepsilon}_{ij}(t) = \dot{\varepsilon}_s \frac{3\sigma_{ij}}{2q} + \left(\frac{3\sigma_m}{2q}\, \dot{\varepsilon}_s \right) \delta_{ij}$$

Returning now to the creep function for PVC, equation (A14) can be written in the form

$$\varepsilon_{ij}(t) = \left(\frac{(1+\nu)}{E}\sigma_{ij} - \frac{3\nu}{E}\sigma_m\, \delta_{ij} \right)\left(1 + \left(\frac{t}{\tau} \right)^n \right) \qquad \text{(A20)}$$

When differentiated this gives

$$\dot{\varepsilon}_{ij}(t) = \frac{n}{\tau^n}\left(\frac{(1+\nu)}{E}\sigma_{ij} - \frac{3\nu}{E}\sigma_m\, \delta_{ij} \right) t^{n-1}$$

This can be identified with equation (A19) if

$$\dot{\varepsilon}_s = \frac{2q}{3} \cdot \frac{n}{\tau^n} \frac{(1+\nu)}{E} t^{n-1}$$

and

$$\dot{\varepsilon}_{sw} = \frac{n\sigma_m}{\tau^n} \cdot \frac{(1-2\nu)}{E} \cdot t^{n-1} \qquad \text{(A22)}$$

Furthermore, in the notation used here to refer to the stress invariants q and σ_m, equation (A16) becomes

$$\bar{\sigma} = \frac{(\beta+1)q}{\sqrt{3}} + \frac{3(\beta-1)\sigma_m}{2\beta} \qquad \text{(A23)}$$

Thus $\dot{\varepsilon}_s$ and $\dot{\varepsilon}_{sw}$ in the time-dependent plasticity model (equation (A17)) can be determined from a knowledge of materials parameters n, τ, ν and E and the creep stress identified by q and σ_m.

(to be continued)

A7 APPLICATION OF A LINEAR VISCOELASTIC MATERIALS MODEL

In this illustration, a finite element analysis is used to calculate the response of a simple component to cyclic loading that excites resonant vibrations in the component. The frequencies and relative amplitudes of the lower frequency resonant modes are determined. For the application considered here, the driving force is assumed to have a constant amplitude of 10 kN over the frequency range of interest although the response to an arbitrary distribution of forcing frequencies could be calculated if the force distribution is known.

The component in this application is a thin-walled, hemispherical shell that is fixed at its circumference to a very stiff foundation. The dimensions of the shell and the mesh used in the analysis are shown in figure 15. The cyclic force is applied to the component through the foundation, and the direction of the force is considered to be normal to the foundation plane. The force is assumed to be sufficiently small that the strains in the shell are at all times within the linear viscoelastic range for the material.

The minimum data requirements for the analysis (see table 2a) are values for the storage and loss components of the dynamic tensile modulus, E' and E", the Poisson's ratio ν and the density ρ of the polymer. Strictly, the Poissons ratio is a complex quantity but a negligible loss of accuracy will generally result from assuming this to be a real number. The simplest analysis requires data for E' and E" at a single frequency and the appropriate temperature and assumes properties are independent of frequency. When the vibration frequencies are within a relaxation region for the polymer, more accurate predictions will be obtained using data measured over the relevant frequency range.

Figure 16 shows comprehensive dynamic property values for a polypropylene homopolymer. Values for E' and tan δ_E = E"/E' are shown over a wide frequency range and at discrete temperatures between -10 °C and 50 °C. These results were obtained using a variety of dynamic mechanical test methods. Data at low frequencies up to 100 Hz were determined using the tensile forced non-resonance method (ISO 6721-4). Between 100 Hz and 5 kHz, the flexural resonance method was used (ISO 6721-3). A modification of this method, in which the specimen was forced to vibrate in a longitudinal resonance mode, enabled data up to 10 kHz to be measured. An ultrasonic wave propagation method (ISO 6721-8) was used to determine values between 1 MHz and 5 MHz.

Calculations are shown in figure 17 of the frequencies and amplitudes of the resonant modes of vibration of the polypropylene shell at a temperature of 20 °C. Curve (a) in figure 15 was obtained using values for E' and E" measured at a single frequency of 10 Hz. The assumption here is that properties do not depend on frequency. For comparison, curve (b) shows the response predicted when data for E' and E" over the frequency range between 0.1 Hz and 100 kHz are employed taken from the curves at 20 °C in figure 16.

The measurement of the comprehensive data set in figure 16 requires a variety of test methods, but data like this are often derived from a much smaller quantity of measured values by assuming equivalence in the frequency and temperature dependence of properties. In this way, data over a wide frequency range are obtained by superposition of E' vs frequency data measured over a narrow frequency range but covering a wide span of temperature. The relaxation mechanism in figure 16 is assigned to the glass-to-rubber transition in the amorphous phase of the polymer and the kinetics of this transition are generally described by

the WLF equation for time-temperature superposition. Indeed, the frequencies of the peaks in tan δ_E satisfy the WLF equation for the temperature dependence of mean relaxation times. However, the breadth of the loss factor curves in figure 16 becomes more narrow as the temperature is raised. This implies that the distribution of relaxation times in this relaxation process changes with temperature. As a consequence, the shape of the E' against frequency curve will change with temperature, and this will limit the accuracy of property values predicted using time-temperature superposition.

A8 APPLICATION OF AN ANISOTROPIC ELASTIC MODEL

An anisotropic linear elastic analysis is used here to derive the stress distribution around a hole in the centre of a laminate under a uniaxial tensile stress. The laminate consists of 8 layers of a unidirectional, continuous fibre reinforced plastic. Coordinate axes and laminate dimensions are shown in figure 18. The x-axis is in the direction of applied stress. The fibre orientation in each layer is identified by the angle that the fibre axis makes with the x-axis and is shown in the enlarged section. Coordinate axes for each layer are defined such that the 1-axis is along the direction of fibre orientation. Properties in the plane transverse to this axis are assumed to be isotropic. The 3-axis is taken to coincide with the through-thickness direction (z-axis) of the laminate.

In the analysis, constraints associated with load introduction are assumed to be localised at each end of the plate so that the material around the hole can be considered to be in a state of plane stress. This implies that there are no components of stress in the laminate along the thickness direction (z-axis).

Because of the assumption of transverse isotropy, 5 independent materials parameters are needed to characterise the elastic anisotropy of a single layer. Table A4 lists 5 properties that are commonly used for this purpose. E_1 and E_2 are tensile moduli along and transverse to the direction of fibre orientation, respectively. G_{12} and G_{23} are shear moduli in a plane containing the fibre axis and in the plane normal to this axis, respectively and ν_{12} is Poisson's ratio for an applied stress along the fibre axis. In table A4, these parameters are identified with properties E_p, E_n, G_p and ν_{pn} that have been introduced in table 2b and section 3.2.

Table A4 also gives measured values for a carbon fibre reinforced epoxy. Properties were determined using specimens cut from a compression moulded plate in which the fibres were aligned in a single direction. Tensile properties and Poisson's ratio were measured using ISO 527-5, and the shear modulus G_{12} was determined using ISO 15310. A knowledge of the transverse shear modulus G_{23} is not needed for this analysis since a state of plane stress exists in the laminate and in each layer. It may be worth noting that these properties can also be determined using ultrasonic wave propagation methods described in ISO 6721-8. The current version of this standard deals with isotropic materials, and the data analysis required for anisotropic materials is not described.

Table A4 - Materials properties for a transversely isotropic carbon fibre reinforced epoxy

$E_1 = E_p$ (GPa)	$E_2 = E_n$ (GPa)	$G_{12} = G_p$ (GPa)	$\nu_{12} = \nu_{pn}$	G_{23}
135	10	5.3	0.3	

A finite element analysis has been used to calculate the distribution of the maximum principal stress in each layer produced by an applied stress of 140 MPa. Contours of maximum principal stress are shown in figure 19. The maximum values of these stresses have been used to explore the validity of using multiaxial failure criteria for an individual layer to predict the onset of failure in the laminate.

ANNEX B

APPLICATION OF PROCESSING SIMULATION ANALYSIS FOR PLASTICS

In this Annex, the application of various processing simulation programs for plastics is illustrated to demonstrate the use of relevant material data identified in clause 4.2. The applications considered in this annex are shown in table B - 1

Table B – 1. Applications of processing simulations considered in this annex

Section	Processing Method	Analysis type
B.1	Injection moulding	B.1.1 Simple mould filling of thermoplastic B.1.2 Advanced filling, packing and cooling of thermoplastics B.1.3 Shrinkage/warpage analysis
B.2	Extrusion	B.2.1 Polymer melting in the extruder B.2.2 Simulation of melt flow in a coat hanger die B.2.3 Simulation of melt flow in a profile die
B.3	Blow moulding	

It is important to note that the simulation programs employ a wide variety of viscosity models to describe the flow behaviour of polymer melt. Typically, each software program determines the appropriate coefficients for the chosen viscosity model, which are derived from the experimental melt shear viscosity data by a suitable curve fitting procedure. The most common viscosity models employed in the simulation of injection molding are listed in Table B – 2. It should be noted that the actual input requirements for the viscosity data might vary depending on the software package. For example, in MOLDFLOW software the input format for viscosity data for the first order model can be in the form of either the three coefficients (viscosity factor, shear factor and temperature factor) or as three (3) data point sets

T_1, $\dot{\gamma}_1$ and η_1; T_2, $\dot{\gamma}_2$ and η_2; T_3, $\dot{\gamma}_3$ and η_3

from which the model coefficients A, B and C are calculated by the software. Likewise for the second order model, the input format for viscosity data can be in the form of either a second order viscosity matrix as shown below or as the six (6) polynomial coefficients.

Temperature (°C)	Shear rate (1/s)	Viscosity (Pa.s)
$T_m - 20$	1000	η_1
T_m	100	η_2
T_m	1000	η_3
T_m	10000	η_4
$T_m + 20$	100	η_5
$T_m + 20$	1000	η_6

Table B - 2. Common viscosity models employed in simulations for injection moulding

Model description	Model	Description of symbols
First order model	$\eta = A\ \dot{\gamma}^{B} \exp CT$ *(commonly used in simple 2 dimensional analysis)*	A = Viscosity factor B = Shear rate factor C = Temperature factor
Second order model	$\ln \eta = A_1 + A_2 (\ln \dot{\gamma}) + A_3 T + A_4 (\ln \dot{\gamma})^2 + A_5 (\ln \dot{\gamma}) T + A_6 T^2$	A_1 = Model coefficient A_2 = Model coefficient A_3 = Model coefficient, 1/°C A_4 = model coefficient A_5 = Model coefficient, 1/°C A_6 = model coefficient, $1/(°C)^2$
Cross/Arrhenius model	$\eta = \frac{B \exp \beta p . \exp T_b / T}{1 + \{(\eta_o \dot{\gamma}) / \tau^*\}^{1-n}}$	η_o = Zero shear viscosity, Pa.s n = Power law exponent τ^* = Shear stress level at which shear thinning begins to manifest itself, Pa T_b = Temperature sensitivity factor, K B = Constant relating to zero shear viscosity, Pa.s β = Factor relating pressure dependence of η_o, 1/Pa p = Pressure, Pa
Cross/WLF model	$\eta = \frac{D_1 \exp[-A_1 (T - T_r) / (A_2 + (T - T_r))]}{1 + \{(\eta_o \dot{\gamma}) / \tau^*\}^{1-n}}$ where $T_r = D_2 + D_3 p$	η_o = Zero shear viscosity, Pa.s n = Power law exponent τ^* = Shear stress level at which shear thinning begins to manifest itself, Pa T_r = Reference temperature, °C D_1 = Constant, Pa-s D_2 = Glass transition temperature at zero pressure, °C D_3 = Pressure sensitivity factor, °C/Pa A_1 = Temperature sensitivity factor of viscosity A_2 = Constant, °C p = Pressure, Pa

η = Viscosity, Pa.s $\dot{\gamma}$ = Shear rate, 1/s T = Temperature, °C

Table B – 3 summarizes the most common viscosity models used in the simulation of processes involving extrusion.

Table B - 3. Common viscosity models employed in extrusion simulations

Model description	Model	Description of symbols
Newtonian model	$\eta = A \exp - b(T-T_r)$	A = Constant, Pa.s b = Temperature sensitivity factor, 1/°C T_r = Reference temperature, °C
Power law model	$\eta = A\ \dot{\gamma}^{\,n-1} \exp - b(T-T_r)$	A = Constant, Pa.s b = Temperature sensitivity factor, 1/°C T_r = Reference temperature, °C n = Power law exponent
Log polynomial model	$\ln \eta = a_1 + a_2 (\ln \dot{\gamma}) + a_3 (\ln \dot{\gamma})^2 + a_4 (T - T_r) + a_5 (T - T_r)^2 + + a_6 (T - T_r) (\ln \dot{\gamma})$	T_r = Reference temperature, °C a_1 = Model coefficient a_2 = Model coefficient a_3 = Model coeffcient a_4 = Model coefficient, 1/°C a_5 = Model coefficient, 1/(°C)^2 a_6 = Model coefficient, 1/°C
Carreau model (simplified form)	$\eta = \frac{A \exp - b(T - Tr)}{[1+(r\dot{\gamma} \exp - b(T-T_r))^a]^{(1-n)/a}}$ $\eta = \frac{\eta_o}{[1+(\lambda\dot{\gamma})^2]^{(1-n)/2}}$	η_o = Zero shear viscosity, Pa.s A = Model constant, Pa.s b = Temperature sensitivity factor, 1/°C T_r = Reference temperature, °C a = Constant r = Constant, s n = Power law exponent λ = Parameter relating to the shear rate for the onset of shear thinning, s η_o = Zero shear viscosity, Pa.s
Cross model	$\eta = \frac{\eta_o}{1+\{(\eta_o\dot{\gamma}) / \tau^*\}^{1-n}}$	τ^* = Shear stress level at which shear thinning begins to manifest itself, Pa n = Power law exponent

η = Viscosity, Pa.s $\dot{\gamma}$ = Shear rate, 1/s T = Temperature, °C

The simplified form of the Carreau model assumes the viscosity to be zero when the shear rate approaches infinity.

The common models employed for pvT data in the simulation programs are illustrated in Table B-4.

Table B – 4. Common pvT models employed in processing simulations

Model description	Model	Description of coefficients
2-domain Tait model (employed by C-MOLD software)	$v(T,p) = v_0(T)\,[\,1 - 0.0894 \ln\{1 + p/B(T)\}] + v_t(T,p)$ where, if $T > T_t(p)$, $v_0 = b_{1m} + b_{2m}(T-b_5)$ $B(T) = b_{3m} \exp - b_{4m}(T-b_5)$ $v_t(T,p) = 0$ and if $T < T_t(p)$ $v_0 = b_{1s} + b_{2s}(T-b_5)$ $B(T) = b_{3s} \exp - b_{4s}(T-b_5)$ $v_t(T,p) = b_7 \exp b_8(T-b_5) - b_9 p$	v = specific volume, m^3/kg T = Temperature, °C p = Pressure, Pa $T_t(p)$ = Transition temperature, °C $= b_5 + b_6 p$ b_{1m}, b_{1s} = Tait coefficients, m^3/kg b_{2m}, b_{2s} = Tait coefficients, m^3/kg. K and if $T < T_t(p)$ b_{3m}, b_{3s} = Tait coefficients, Pa b_{4m}, b_{4s} = Tait coefficients, 1/K b_5 = Tait coefficient, K b_6 = Tait coefficient, K/Pa b_7 = Tait coefficient, m^3/kg b_8 = Tait coefficient, 1/K b_9 = Tait coefficient, 1/Pa
2-region model (employed by MOLDFLOW software)		
<u>semicrystalline material</u>		
in the lower temperature region (below T_g)	$v = \frac{a_1}{a_4+p} + \frac{a_2 T}{a_3+p} + a_5 \exp(a_6 T - a_7 p)$	a_i = Tait coefficients
in the upper temperature region (above (T_g)	$v = \frac{b_1}{b_4+p} + \frac{b_2 T}{b_3+p}$	b_i = Tait coefficients
and boundary equation	$P = c_1 + c_2 T$	c_i = Tait coefficients
<u>amorphous material</u>		
in the lower temperature region (below T_g)	$v = \frac{a_1}{a_4+p} + \frac{a_2 T}{a_3+p}$	
in the upper temperature region (above (T_g)	$v = \frac{b_1}{b_4+p} + \frac{b_2 T}{b_3+p}$	

The input for the pvT data in MOLDFLOW software utilizes a set of 13 standard points to describe the pvT behaviour of a semicrystalline material - seven (7) of these standard points are chosen in the lower temperature region, and four (4) standard points in the upper temperature region with the two (2) remaining standard points relating to boundary points. For an amorphous material, on the other hand, a set of only 10 standard points are utilized - four (4) standard points each in the lower and upper temperature region with the two (2) remaining standard points relating to boundary points. The program reads these standard points and determines the corresponding Tait coefficients described in table B – 4.

B1 SIMULATION OF THE INJECTION MOULDING PROCESS

To illustrate the influence of material data for processing simulation, it is important to consider each scenario discussed in clause 4.2 separately.

Illustration of simple mould filling analysis of thermoplastics

To illustrate the use of the material data in simple mould filling analysis of thermoplastics, a single component geometry - an automotive door panel - as shown in figure B-1 is chosen. The part dimensions and the runner system in the illustration correspond closely to the actual dimensions of the component on a vehicle today. In particular, the thickness of the part is 2.25 mm and the runner system consists of a hot runner with a diameter of 16 mm, tapered having a diameter ranging from 10 mm to 5 mm while the fan gate thickness varies from an initial thickness of 4 mm to a junction thickness of 1.5 mm.

The finite element mesh of the part and the runner system was created using shell and beam elements (Figure B-2).

Simulations were carried out using the viscosity data (generated in accordance with ISO 11443) with and without corrections for the non-Newtonian behaviour and juncture loss effects. The three cases considered correspond to using apparent viscosity data without any corrections, with Rabinowitsch correction only (correction for the non-Newtonian behaviour) and with both Rabinowitsch and Bagley corrections (for the juncture losses). In each case, the material viscosity is represented by the Cross/Arrhenius model.

The material data input needed for the simple mould filling analysis (see Table 3a in section 4.2.2) are as follows:

ρ_m	728	kg/m^3
c_{pm}	3400	J/kg °C
k_m	0.169	W/m °C
T_r	130	°C

The software package used in this illustration, C-MOLD, uses the transition temperature instead of T_s and T_{ej}.

The Cross/Arrhenius model coefficients for viscosity data are listed below:

Case i.	Apparent viscosity data	n = 0.25122		
		τ^* = 51845	Pa	
		B = 0.012998		Pa-s
		T_b = 5498.5	K	
		β = 0	1/Pa	
Case ii.	With Rabinowitsch correction only	n = 0.25208		
		τ^* = 43216	Pa	
		B = 0.014934	Pa-s	
		T_b = 5396.3	K	
		β = 0	1/Pa	
Case iii.	With Rabinowitsch and Bagley corrections	n = 0.22698		
		τ^* = 45319	Pa	
		B = 0.0099708	Pa-s	
		T_b = 5549.7	K	
		β = 0	1/Pa	

Figure B-3 shows the viscosity vs. shear rate data at different temperatures for the three cases. The following process conditions are used for the filling stage simulation:

Melt temperature	240°C
Mould temperature	30°C
Fill time	4s
Injection speed profile (relative)	constant during filling
Filling/Packing switch over	at 97% volume

A comparison between the experimental observation of melt front advancement from a series of short shots and the result of the numerical simulation in the case without any corrections is shown in figure B-4 and demonstrates a good correlation between numerical simulation and experiment in terms of melt front description. The influence of the corrections on pressure distribution for the three cases are shown in figures B-5 through B-7. The differences in term of maximum pressure (important for the determination of the machine size and in terms of

aspect and mechanical quality of the final part) is worth noting. The 17% difference in maximum pressure obtained between the cases i and iii - without correction and with complete corrections - clearly illustrates the importance of taking into consideration the corrections to the viscosity data on the final results of moulding simulation and, consequently, on the prediction of the final part properties.

Illustration of advanced mould filling, packing and cooling analysis of thermoplastics

Use of the material data in advanced mould filling, packing and cooling analysis of thermoplastics is illustrated with the example of an automotive rocker cover (see figure B-8). The part dimensions are 500 mm x 250 mm x 100 mm with a total volume of 953.5 cm^3 and a global thickness of 3.0 mm while the local thickness ranges between 1.5 mm (ribs) and 2.5 mm (flange). The material selected for the rocker cover is MINLON® EFE6053 from DuPont Engineering Polymers, a PA 66 grade containing 24 % glass fiber and 16 % mineral filler. The material data input required for the advanced filling, packing and cooling analysis using MOLDFLOW software program (see Table 3b in section 4.2.2) is as follows:

c_{pm}*	2554	J/kg °C
k_m*	0.2714	W/m °C
T_s	235	°C
T_{ej}	203	°C

* Although the input for c_p and k in advanced filling analysis may require values as a function of temperature (Table 3b), for simplification, single values corresponding to the melt state are used for this illustration.

A second order model was used to represent the material viscosity. The second order viscosity matrix input values for this material are:

® Registered Trademark of E I DuPont de Nemours

Temperature (°C)	Shear Rate (1/s)	Viscosity (Pa.s)
275	1000	285.6
295	100	279.8
295	1000	147.6
295	10000	48.3
315	100	130.2
315	1000	76.8

The 13 standard data point input values for pvT data are,

Pressure (MPa)	Temperature (°C)	Specific Volume (m^3/kg)
0	0.0	0.00066725
160	0.0	0.00065427
0	20.0	0.00067184
160	20.0	0.00065671
0	245.2	0.00073382
80	252.1	0.00071306
160	256.3	0.00069784
0	261.0	0.00075958
160	269.9	0.00071500
0	270.0	0.00076297
160	270.0	0.00071501
0	310.0	0.00077803
160	310.0	0.00072409

The Tait model coefficients for the pvT data are computed by the program from these input parameters.

The processing conditions used in the simulation are

Melt temperature	295 °C
Mould temperature	90 °C.
Injection time	2.5 s
Flow rate	377 cm^3/s

At 82% filling, an injection pressure of 100 MPa is reached. At this stage the injection pressure is kept constant which leads to a reduced flow-rate of 32.5 % at 100 % filling after 3.0 s.

Figures B-9 to B-12 show the results of the filling analysis for a balanced runner system with 2 gates each having identical dimensions of 2.0 mm diameter and 2.0 mm length. The initial pressure drop over the runners and gates was computed to be 20 MPa. Due to shear heating the flow-front temperatures increase from 295 °C (melt temperature) to 302.8 °C, (see also figure B-11) - a temperature increase of almost 8 °C. Employing a slower injection rate looks like an obvious option, however, the amount of frozen layer thickness will increase in that case much higher than the 72 % as obtained with 3.0 s injection time, see figure B-12. Proper packing of the areas with the highest amounts of frozen layer can then become difficult.

For the packing analysis, the packing pressure was decreased linearly from 100 MPa at the end of filling to 60 MPa in 4 s and reduced to 0 MPa, in the next 1 s, accounting for a total packing time of 5 s. The computed results are shown in figures B-13 and B-14. Figure B-13 shows the pressure distribution in each of the elements of the model during the 5 s packing interval while figure B-14 shows the amount of frozen layer thickness in % at the end of packing. Though some thick elements still contain molten material in their central layer, it is obvious that after 5 s further packing makes less sense because some cover sections are almost completely frozen.

The cooling analysis was based on the results of the filling analysis, assuming a packing time of 5 s, a cooling time of 25 s and a clamp-open time of 5 s. Figure B-8 shows the three (3) cooling circuits, (diameter of 10 mm), designed for this part. The cooling circuits are assumed to be placed in a cavity made out of P20 steel, or a material with a similar thermal conductivity. In each of the circuits a flow rate of 10 l/min of water is assumed, with an inlet temperature of 80 °C, (compared with estimated mean cavity temperature of 90 °C).

Figure B-15 shows the maximum temperatures, (usually close to the central layers of the elements). It can be seen, that the 12 mm and 8 mm thick runners clearly have the highest temperatures. After 25 s the maximum temperature in the cover still is about 220 °C, at the 5 mm thick rings in the 4 holes in the cover. In order to avoid too much deformation of the cover due ejection forces, (dependant on the placement of the ejector pins), a longer cooling time might be appropriate.

Figure B-16 shows the average temperatures over the thickness after 25 s cooling time and figure B-17 shows the temperature difference between the top and bottom surfaces of the elements of the model. In the latter figure, the red elements thus have a much hotter top surface and the blue elements a much hotter bottom surface. Better cooling of these spots may not only result in a reduced cycle time, but also in less warpage because of more uniform temperatures at ejection.

B1.3 Illustration of shrinkage/warpage analysis

The use of material data in shrinkage/warpage analysis will be illustrated with the same automotive rocker cover part as described in Annex B.1.3 using the shrinkage/warpage analysis software of MOLDFLOW. This software normally uses shrinkage coefficients as measured by MOLDFLOW, however, one can modify these coefficients in a user-database.

For the material used in this illustration, MINLON EFE6053 from Du Pont Engineering Polymers, – PA 66 grade containing 24 % glass fiber and 16 % mineral filler - the shrinkage components due to crystallinity, volumetric shrinkage and shrinkage due to mold restraints are less important than the shrinkage due to fibre orientation.

The material data input for the shrinkage/warpage analysis (see Table 3d in section 4.2.2) is as follows:

E_p	8250 MPa
E_n	6000 MPa
ν_{pn}	0.35
ν_{np}	computed from E_p, E_n and ν_{pn} values by the software
G_p	computed from E_p, E_n and ν_{pn} values by the software
a5	0.0034 (corresponding to S_{Mp} = 0.34 %)
b5	0.011 (corresponding to S_{Mn} = 1.1 %)

All other shrinkage coefficients were set to 0.0, thus giving each element the same shrinkage although in different directions. It was further assumed that the cavity had a uniform surface temperature at ejection.

For the definition of the reference planes for the computed deformations (zero deformations, boundary conditions), the following constraints were set:

- for X-deformations (i.e. shrinkage in length direction): one corner point near gate at long, straight edge
- for Y-deformations (i.e. shrinkage in width direction): two corner points at long, straight edge
- for Z-deformations (i.e. warpage of seal face): three corner points at long, straight edge and at short edge of gates

The results of the shrinkage/warpage analysis are presented in figures B–18 and B-19. From figure B-18, the computed shrinkage for the rocker cover over the long straight edge shown to be equal to 0.46 % compared with a shrinkage of 0.34 % parallel to flow. From figure B-19, it follows that the computed warpage is 3.2 mm (displacement of corner 4 versus other 3 corners, which are fixed).

B2 SIMULATION OF THE EXTRUSION PROCESS

The illustrations in this section are intended to demonstrate the use of relevant material data in the simulation of polymer melt flow in two different types of dies – a coat hanger die commonly used in sheet extrusion and a profile die typically used in the extrusion of plastic profile shapes. Independent of the extruded shape itself – sheet, film or profile – the first step involved is the analysis of polymer melting in the extruder. The analysis involves 3 steps:

transport of the solid particles of polymer by drag induced flow with isothermal heat transfer
melting of the polymer particles
isothermal incompressible flow of the homogeneous melt

B2.1 Illustration of analysis of polymer melting in the extruder

In the illustration of the analysis of polymer melting in the extruder here using a conventional screw geometry with a smooth barrel the material chosen is an PE-LD resin. Besides the inputs for various parameters associated with the screw and barrel configurations, the material data inputs required for the analysis (see Table 4 in section 4.2.2) are as follows:

μ_b*	0.3 (assuming a smooth barrel)	
μ_s*	0.25 (assuming a smooth screw surface)	
T_m	110 °C	
ρ_m	775	kg/m^3
ρ_s	919	kg/m^3
ρ_b	595	kg/m^3
c_{pm}**	2700	J/kg °C
c_{ps}**	2595	J/kg °C
k_m**	0.18	W/m °C
ΔH_f	129785 J/kg	

* The dynamic friction coefficients, μ_b and μ_s, are generally difficult to measure. Very often, the roughness of the barrel and screw surface is accounted for in the value of these parameters. For μ_b, a common practice is to use a value of 0.3 for a smooth barrel, 0.45 for a rough barrel and 1.00 for a grooved barrel. Similarly, a value of 0.25 for a smooth screw surface and 0.35 for a corroded screw surface is used as default value for μ_s.

** Although generally the input for c_p and k requires values as a function of temperature, for simplification, single values corresponding to melt and solid state are used for this illustration.

The material viscosity, η (T, $\dot{\gamma}$) is represented by the selected viscosity model, which in this case is Carreau model. The model coefficients for this PE-LD resin are as follows:

A = 6500 Pa.s

b = 0.018 1/°C

r = 1 s

a = 2

n = 0.48

T_r = 180 °C

The flow analysis involves finite difference computations allowing estimation of bulk temperature, distributions of pressure and shear stress, and the energy flux between the barrel and the material along the extruder length for a given mass flow rate. Figure B-20 illustrates the computed bulk temperature along the screw length while the distributions of average pressure and shear stress along the screw length are shown in figures B-21 and b-22 respectively. Figure B-23 illustrates the distribution of computed total energy flux between the barrel and the material.

B2.2 Illustration of the analysis of sheet extrusion process – polymer melt flow in a coat hanger die

The analysis of a sheet extrusion process is illustrated with the same PE-LD material as that used in section B.2. The polymer melting analysis in the extruder is the same as described in B.2. above. A coat hanger die is chosen for the simulation of polymer melt flow in the die. Finite difference computations in the die allow estimation of bulk temperature, pressure and average residence time distributions in the die for a given mass flow rate. The results are shown in figures B-24 to B-26.

B2.3 Illustration of the analysis of profile extrusion process – polymer melt flow in a profile die

The analysis of a profile extrusion process is illustrated with a simple T-shaped profile. A conventional screw geometry with a smooth barrel is selected with the material chosen being PVC. The material data inputs required for the polymer melting analysis in the extruder (see Table 4 in section 4.2.2) are as follows:

μ_b*	0.3 (assuming a smooth barrel)	
μ_s*	0.25 (assuming a smooth screw surface)	
T_{melt}	190 °C	
ρ_m	1050	kg/m^3
ρ_s	1340	kg/m^3
ρ_b	530	kg/m^3
c_{pm}**	2200	J/kg °C
c_{ps}**	2320	J/kg °C
k_m**	0.182	W/m °C
ΔH_f	0	J/kg (amorphous material)

* Very often, the roughness of the barrel and screw surface is accounted for in the value of these parameters. For μ_b, a common practice is to use a value of 0.3 for a smooth barrel, 0.45 for a rough barrel and .00 for a grooved barrel. Similarly, a value of 0.25 for a smooth screw surface and 0.35 for a corroded screw surface is used as default value for μ_s.

** Although generally the input for c_p and k requires values as a function of temperature, for simplification, single values corresponding to melt and solid state are used for this illustration.

Using a log polynomial viscosity model for PVC, the data inputs for the coefficients are as follows:

$a_1 = 11.784$
$a_2 = -0.6391$
$a_3 = -1.12744$ E-02
$a_4 = -1.83449$ E-02 1/°C
$a_5 = 8.78448$ E-06 $1/(°C)^2$
$a_6 = 9.66512$ E-04 1/°C
$T_r = 0$ °C

Since polymer melting analysis has already been described in section B.2.1, only the simulation of polymer melt flow in the profile die is presented here. Finite difference computations allow estimation of total stress, shear rate, and velocity distributions in the die for a given mass flow rate. The results are shown in figures B-27 to B-29.

B3 SIMULATION OF BLOW MOLDING PROCESS

To be included later

B4 SIMULATION OF BLOWN FILM EXTRUSION PROCESS

To be included later

FIGURE CAPTIONS

Figure 1 Component geometry and loading arrangement selected to illustrate the application of different materials models with finite element methods.

Figure 2 Diagram of the meshes used for the finite element analyses.

Figure 3 Results for the engineering tensile stress and the Poisson's ratio with tensile strain for a propylene copolymer. The true tensile stress has been calculated from these results.

Figure 4 Calculated variation of the force with the central deflection obtained with a linear elastic analysis. Comparison is made with calculations based on a non-linear analysis (see figure 9).

Figure 5 Contours of tensile strain in the radial direction at a central deflection of 4 mm predicted using a linear elastic analysis.

Figure 6 Variation of the force with the central deflection predicted using a non-linear, elastic analysis.

Figure 7 Contours of tensile strain in the radial direction at a central deflection of 4 mm predicted using a non-linear elastic analysis.

Figure 8 True yield stress and plastic component of Poisson's ratio with the true plastic component of strain derived from the data in figure 3 (see equations (A6), (A7) and (A9).

Figure 9 Force/deflection curves calculated using von Mises and linear Drucker-Prager models.

Figure 10 Contours of tensile strain in the radial direction at a central deflection of 12 mm calculated using (a) the von Mises model and (b) the linear Drucker-Prager model.

Figure 11 True stress/true strain curves for a propylene copolymer obtained at different strain rates. The rates indicated are for the plastic strain component.

Figure 12 Force/deflection curves calculated for a range of loading speeds using the rate-dependent material properties shown in figure 11.

Figure 13 Tensile creep compliance curves for PVC at different levels of applied stress. Creep behaviour is modelled using equations (A12) and (A13) in which the effects of physical ageing have been neglected.

Figure 15 Finite element mesh and dimensions used for the calculation of resonance frequencies of a hemispherical shell of a viscoelastic material.

Figure 16 Frequency dependence of E' and tan δ_E for polypropylene at temperatures indicated on each curve.

Figure 17 Velocity amplitudes and frequencies of the resonant modes of the hemispherical shell shown in figure 15. Curve (a) was obtained using dynamic property data from figure 16 at a single frequency of 10 Hz. Curve (b) was obtained using data over the whole frequency range.

Figure 18 Schematic diagram of the laminate showing the configuration of the layers and the mesh used for the finite element analysis.

Figure 19 Contours of maximum principal stress (MPa) in each layer produced by a remote stress on the laminate of 140 MPa.

Figure B-1 Automotive door panel geometry and runner system.

Figure B-2 Finite element mesh used for the simple injection molding simulation of the automotive door panel.

Figure B-3 Representation of Viscosity vs. shear rate data at different temperatures for the three cases.

Figure B-4 Comparison of the experimental short shots and the numerical simulation melt front advancement.

Figure B-5 Pressure distribution at the end of filling stage for case i (using the apparent viscosity).

Figure B-6 Pressure distribution at the end of filling stage for case ii (using the modified viscosity with Rabinowitsch correction only).

Figure B-7 Pressure distribution at the end of filling stage for case iii (using the modified viscosity with Rabinowitsch and Bagley corrections).

Figure B-8 Model of the rocker cover illustrating the finite element mesh and cooling lines.

Figure B-9 Computed melt front position versus time for the rocker cover.

Figure B-10 Pressure distribution at end of filling (i.e. start of packing).

Figure B-11 Computed temperatures for the melt flow-front, when passing through the cover.

Figure B-12 Computed frozen layer thickness (%) at end of filling.

Figure B-13 Computed (maximum) pressure during packing.

Figure B-14 Computed frozen layer thickness at end of (5 s) packing.

Figure B-15 Computed maximum temperatures over thickness after 25 s cooling.

Figure B-16 Computed average temperature over thickness after 25 s cooling.

Figure B-17 Computed temperature difference (top-bottom) after 25 s cooling.

Figure B-18 Computed deformations in X-direction for the rocker cover.

Figure B-19 Computed deformations in Z-direction (warpage) for the rocker cover.

Figure B-20 Computed bulk temperature distribution along the screw length.

Figure B-21 Computed average pressure distribution along the screw length.

Figure B-22 Computed distribution of shear stress at the screw surface along the screw length.

Figure B-23 Computed distribution of total energy flux between the barrel and the material along the screw length.

Figure B-24 Computed bulk temperature distribution in the coat hanger die.

Figure B-25 Computed pressure distribution in the coat hanger die.

Figure B-26 Computed average residence time distribution in the coat hanger die.

Figure B-27 Computed total stress distribution in the profile die.

Figure B-28 Computed shear rate distribution in the profile die.

Figure B-29 Computed velocity distribution in the profile die.

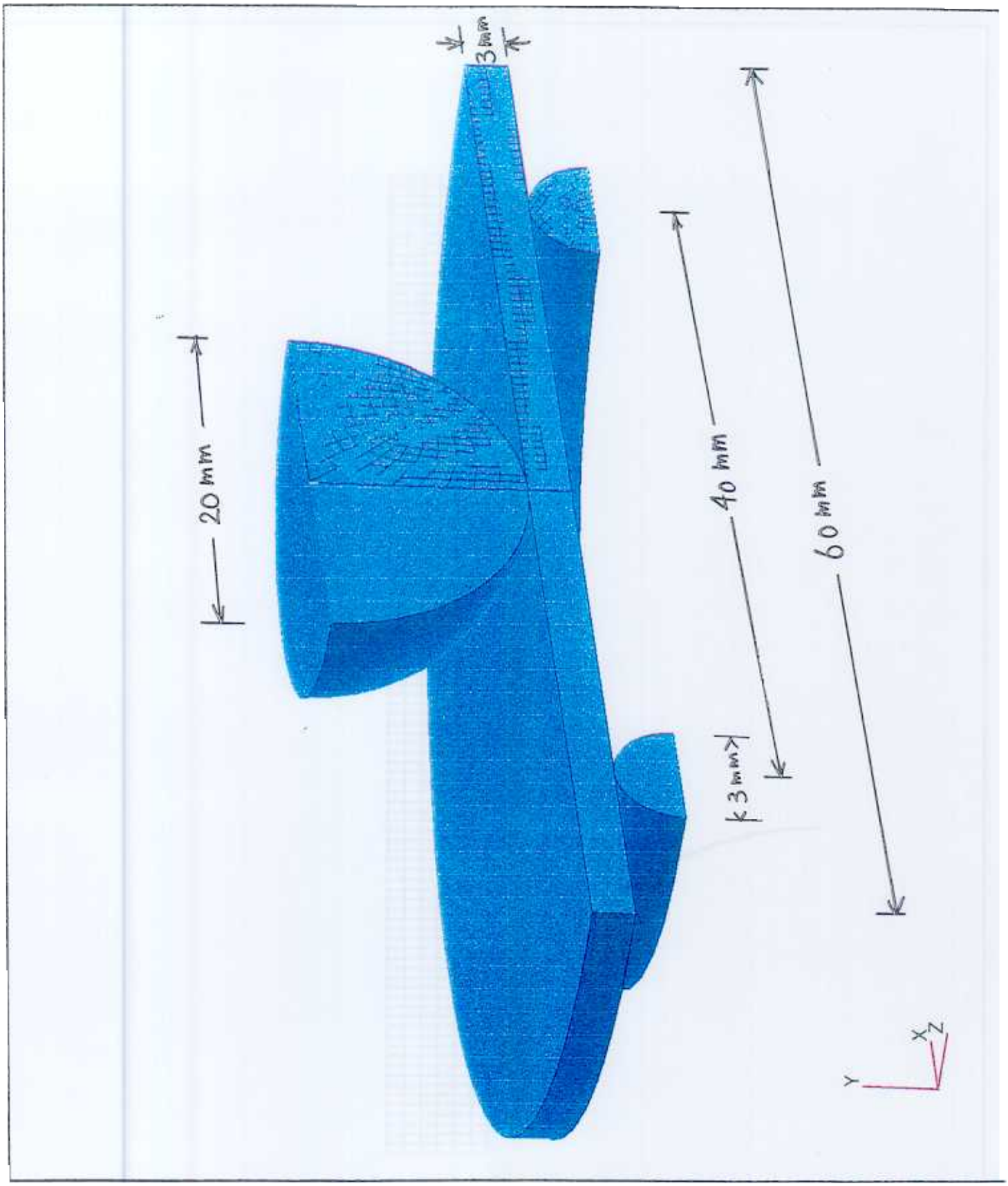


Figure 1 Component geometry and loading arrangement selected to illustrate the application of different materials models with finite element methods.

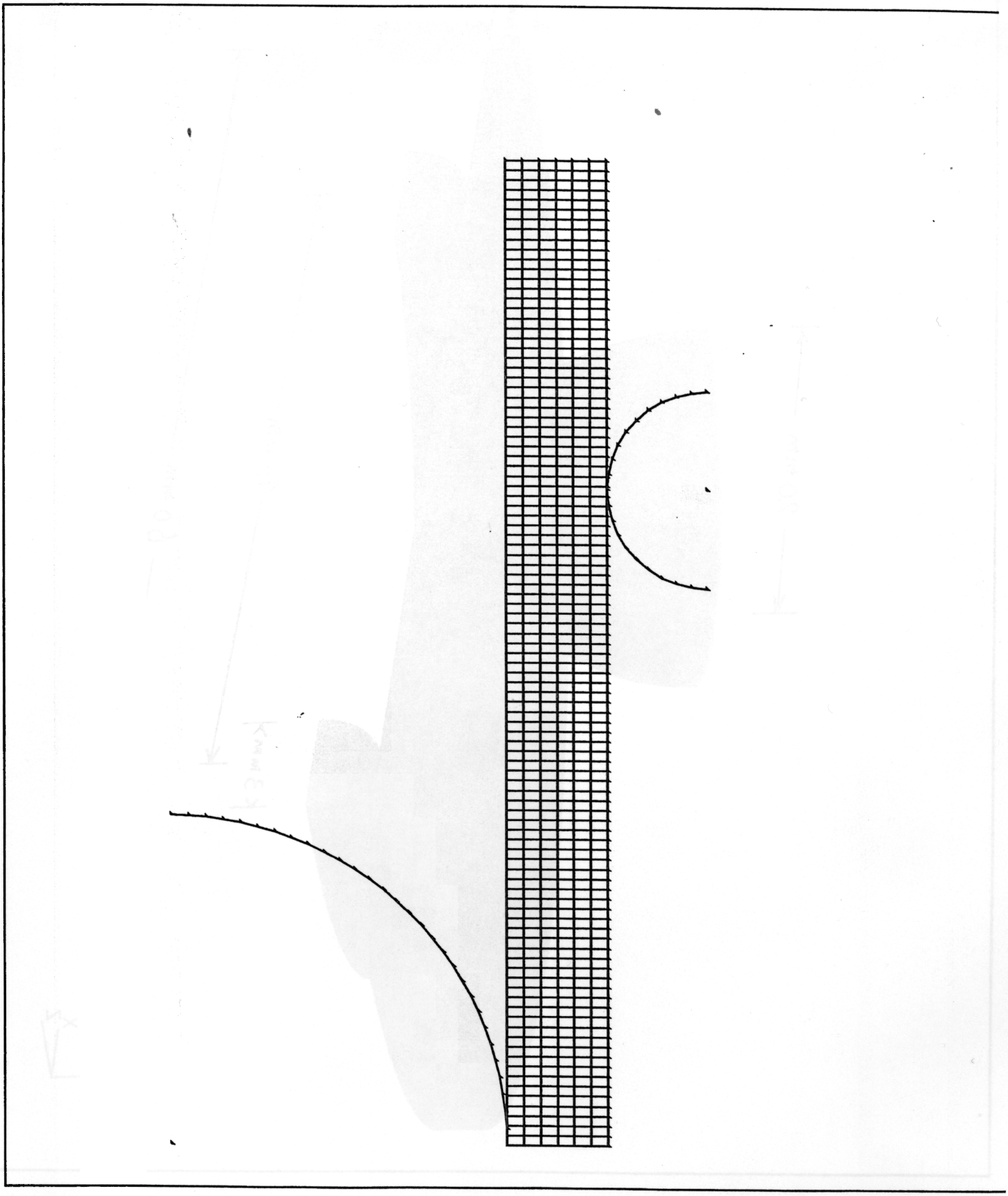


Figure 2 Diagram of the meshes used for the finite element analyses.

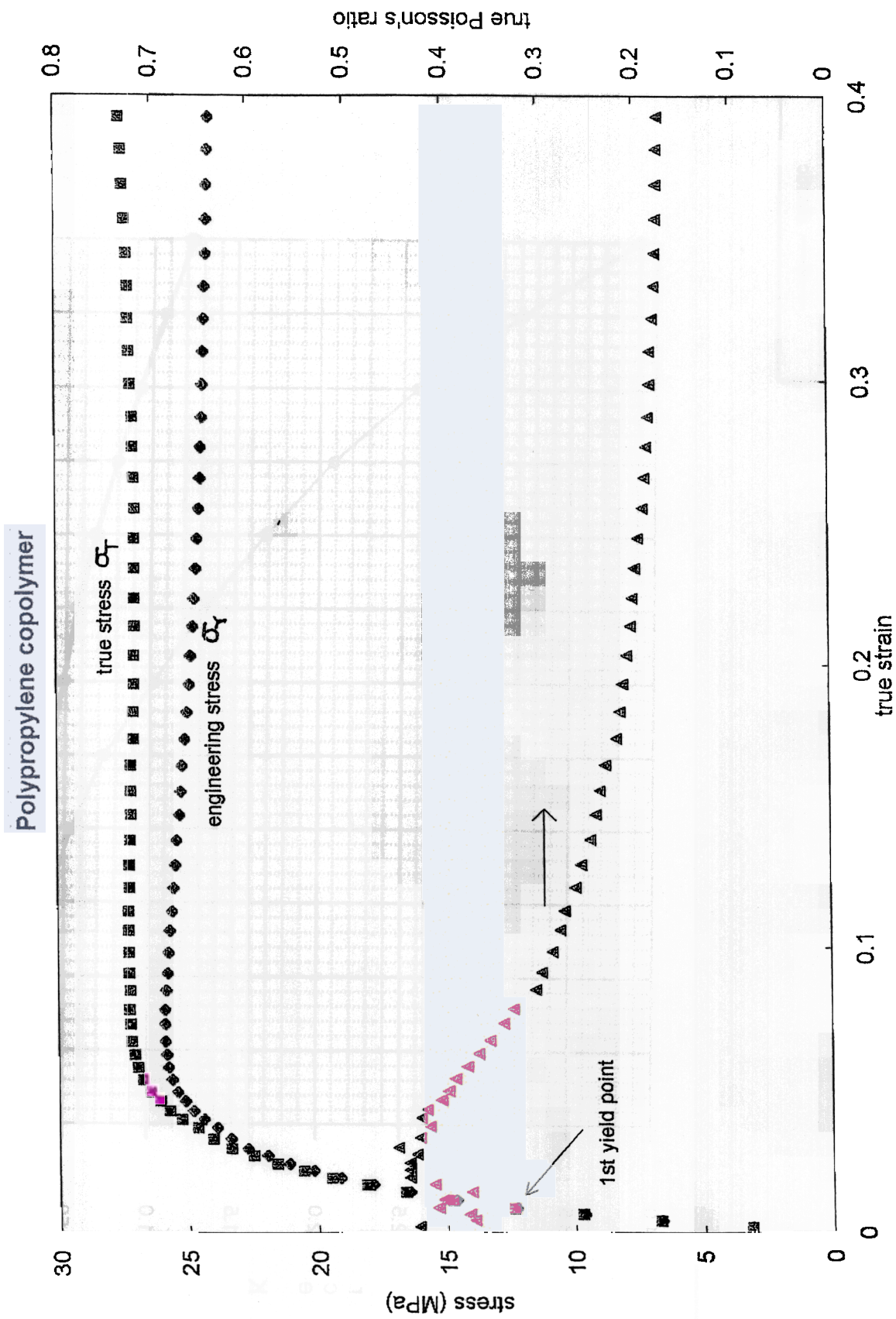


Figure 3 Results for the engineering tensile stress and the Poisson's ratio with tensile strain for a propylene copolymer. The true tensile stress has been calculated from these results.

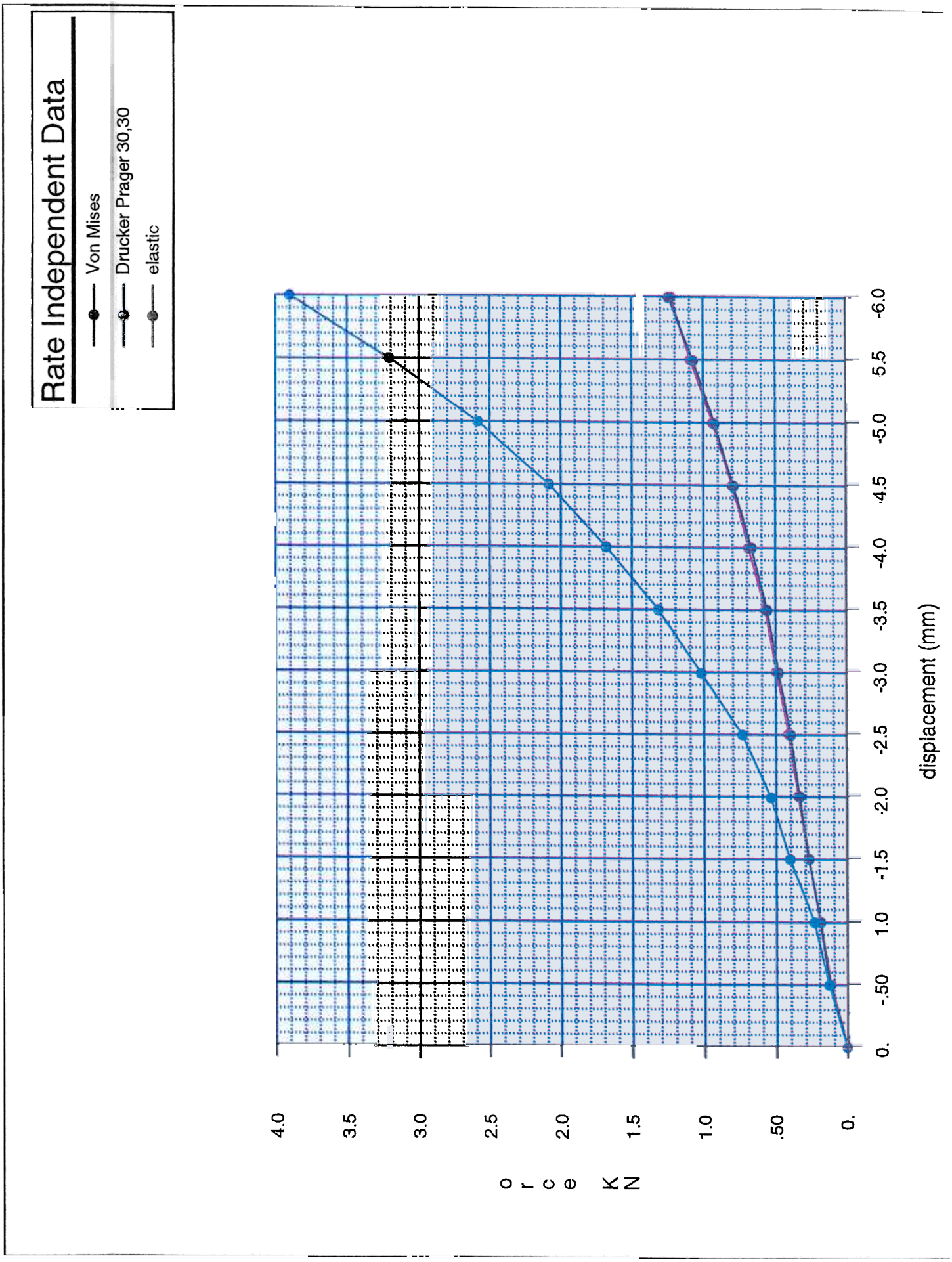


Figure 4 Calculated variation of the force with the central deflection obtained with a linear elastic analysis. Comparison is made with calculations based on a non-linear analysis (see figure 9).

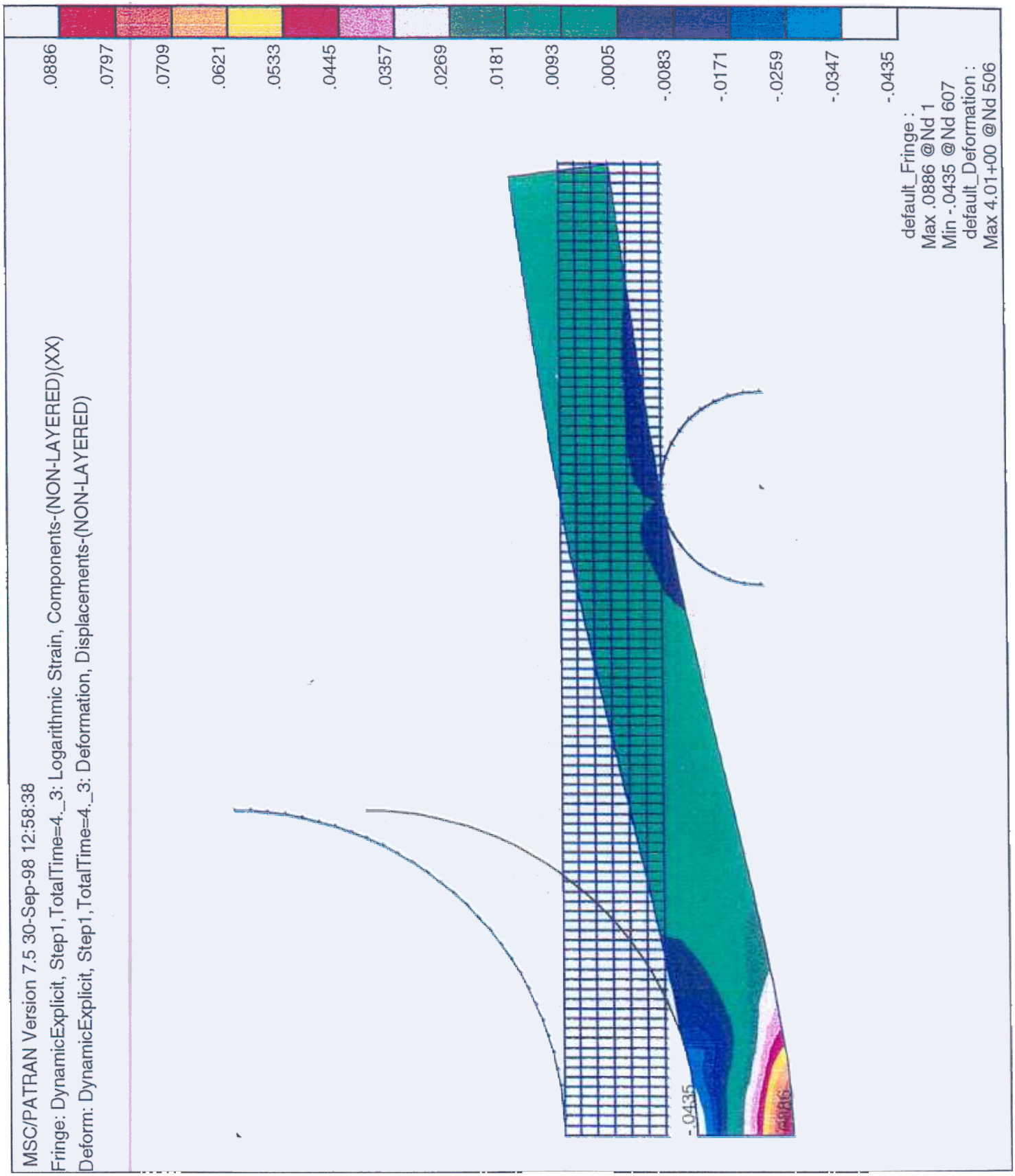


Figure 5 Contours of tensile strain in the radial direction at a central deflection of 4 mm predicted using a linear elastic analysis.

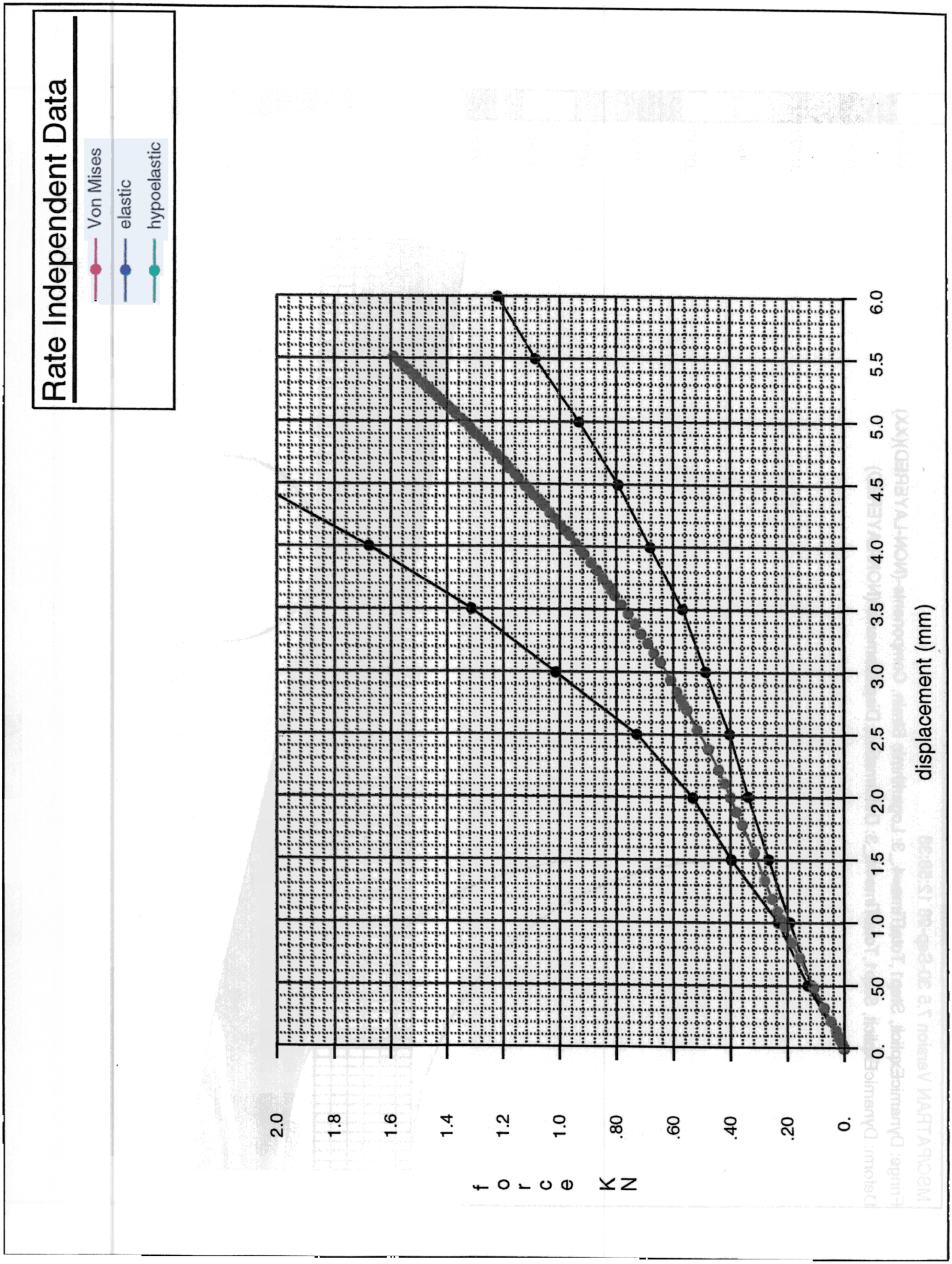


Figure 6 Variation of the force with the central deflection predicted using a non-linear, elastic analysis.

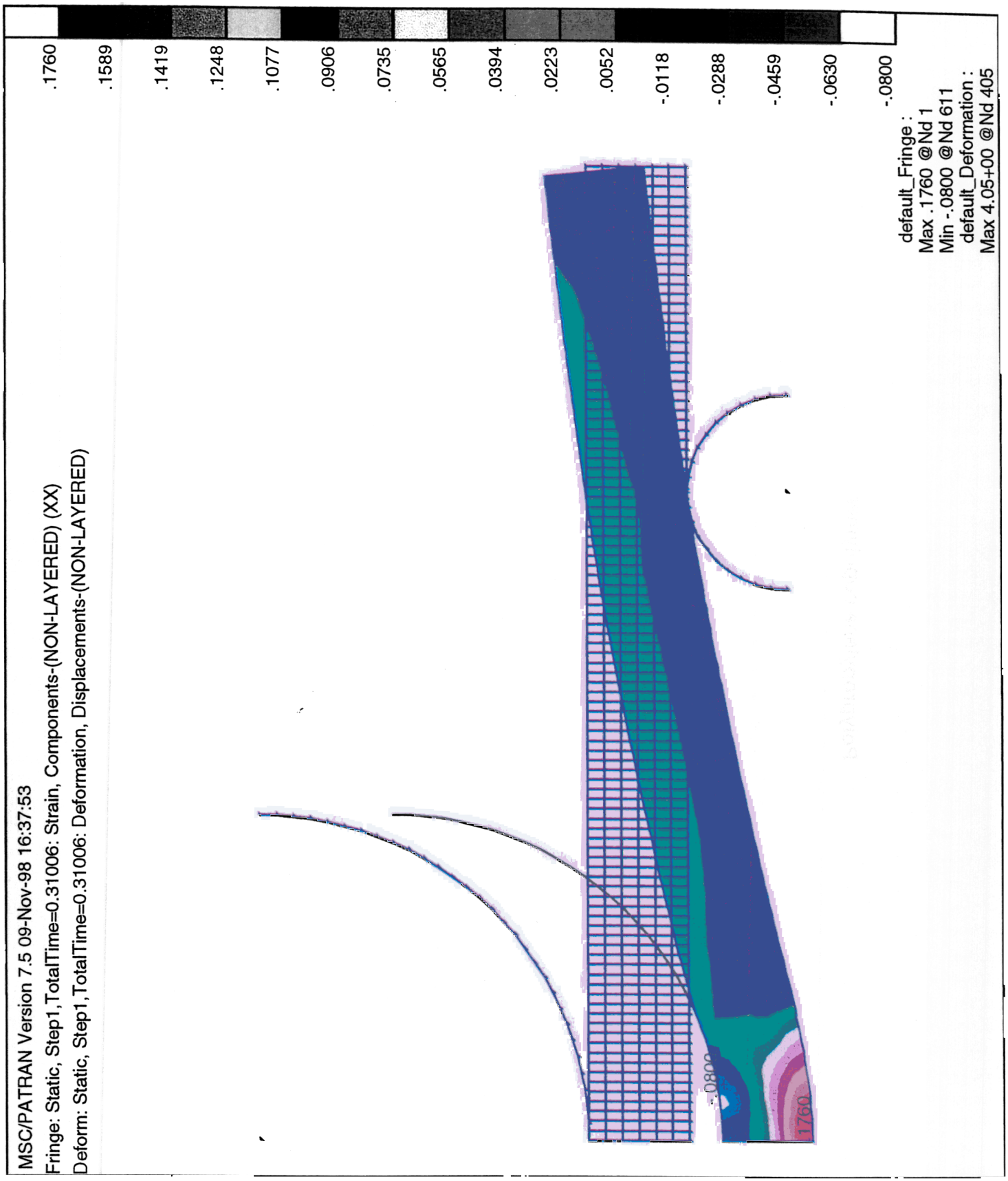


Figure 7 Contours of tensile strain in the radial direction at a central deflection of 4 mm predicted using a non-linear elastic analysis

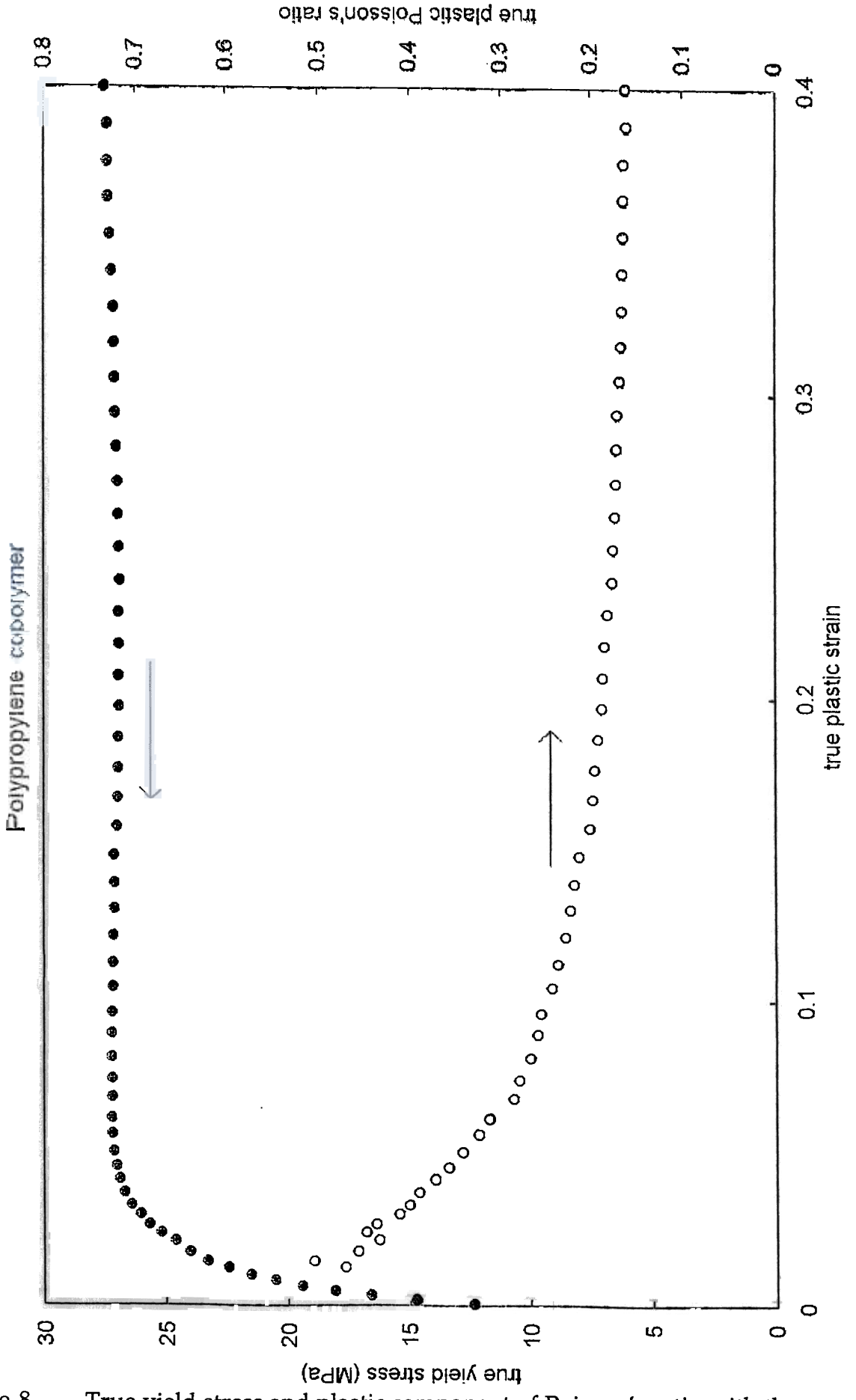


Figure 8 True yield stress and plastic component of Poisson's ratio with the true plastic component of strain derived from the data in figure 3 (see equations (6), (7) and (9).

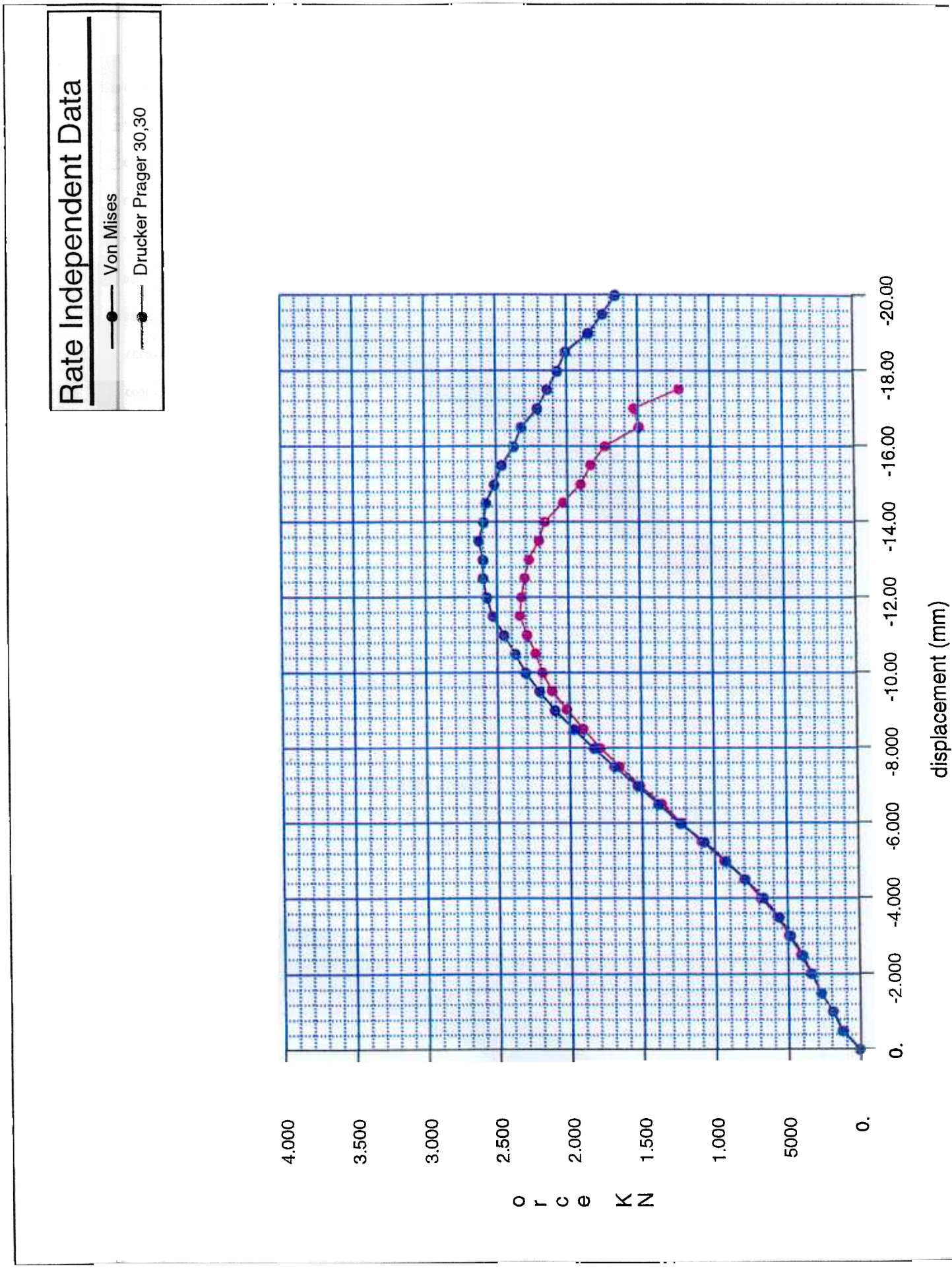
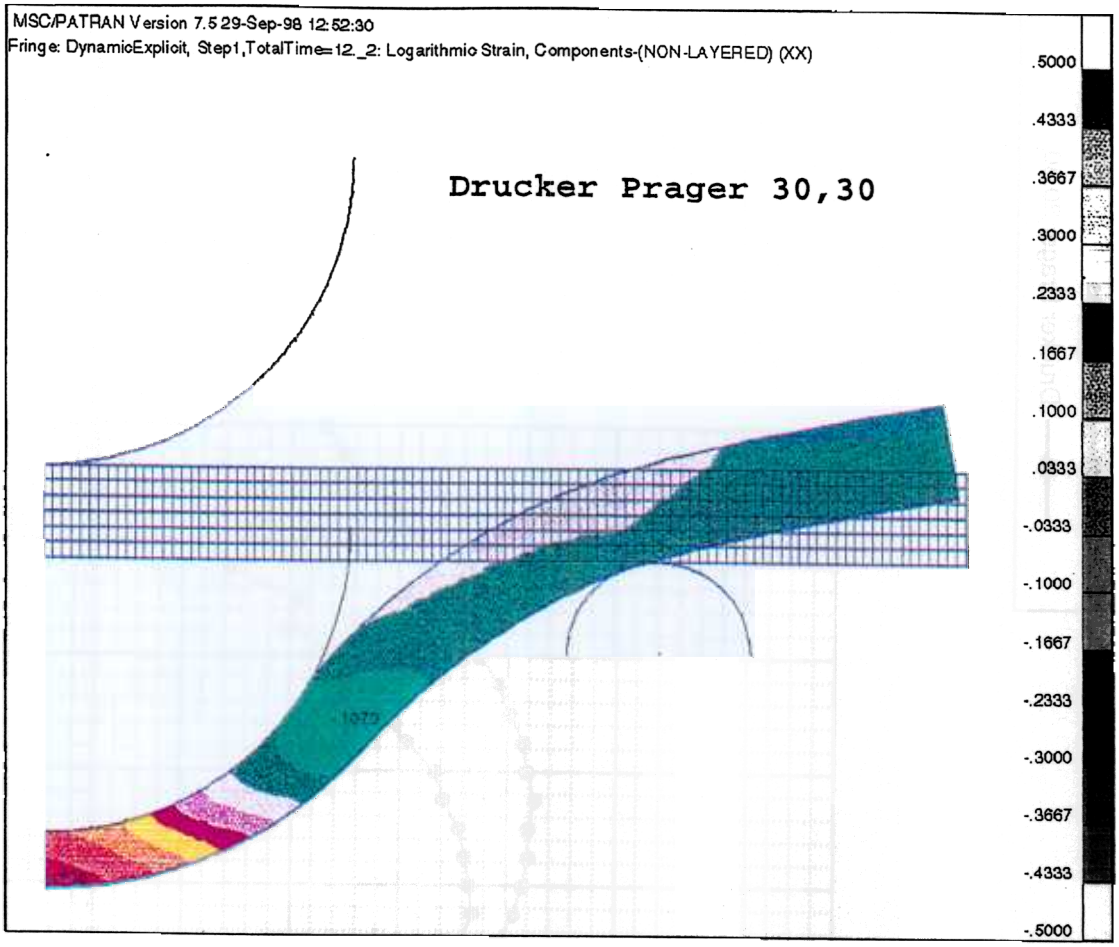


Figure 9 Force/deflection curves calculated .g von Mises and linear Drucker-Prager models.



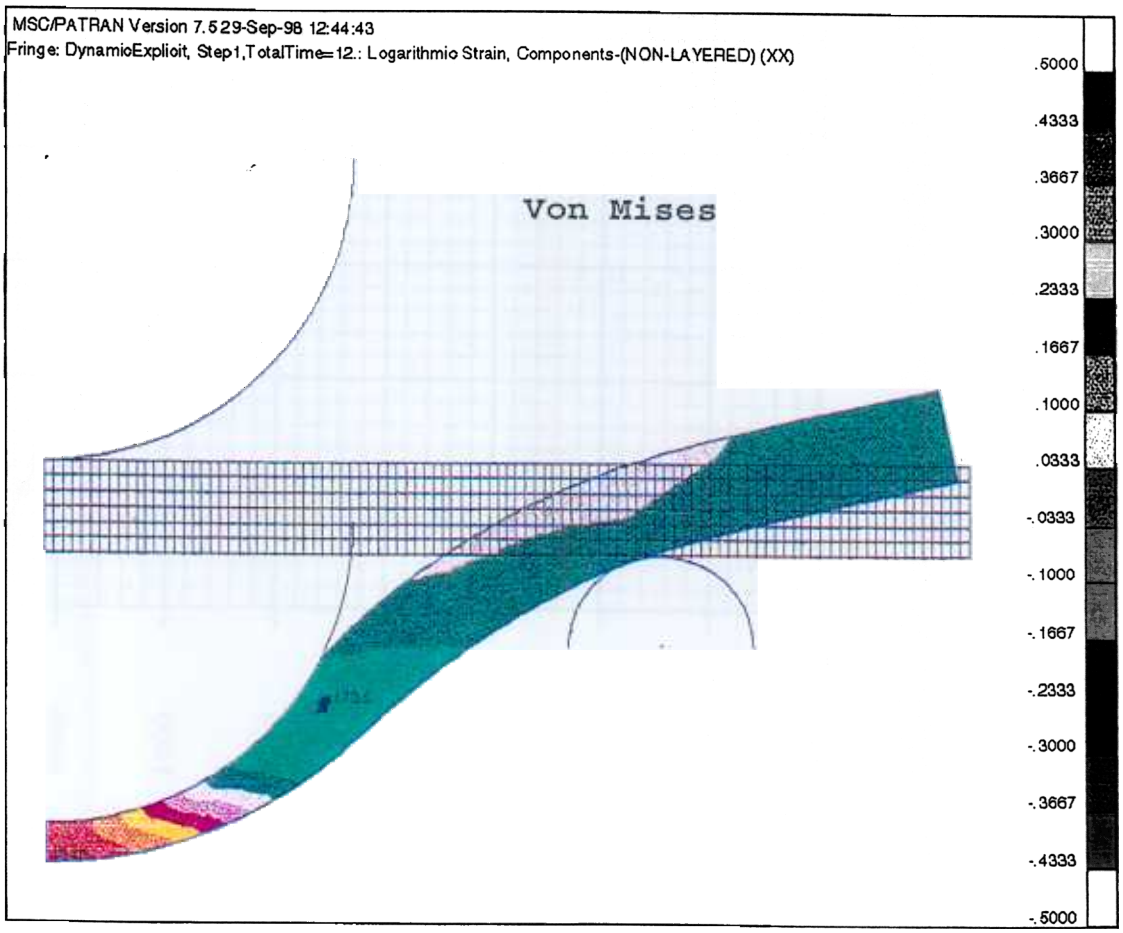


Figure 10 Contours of tensile strain in the radial direction at a central deflection of 12 mm calculated using (a) the von Mises model and (b) the linear Drucker-Prager model.

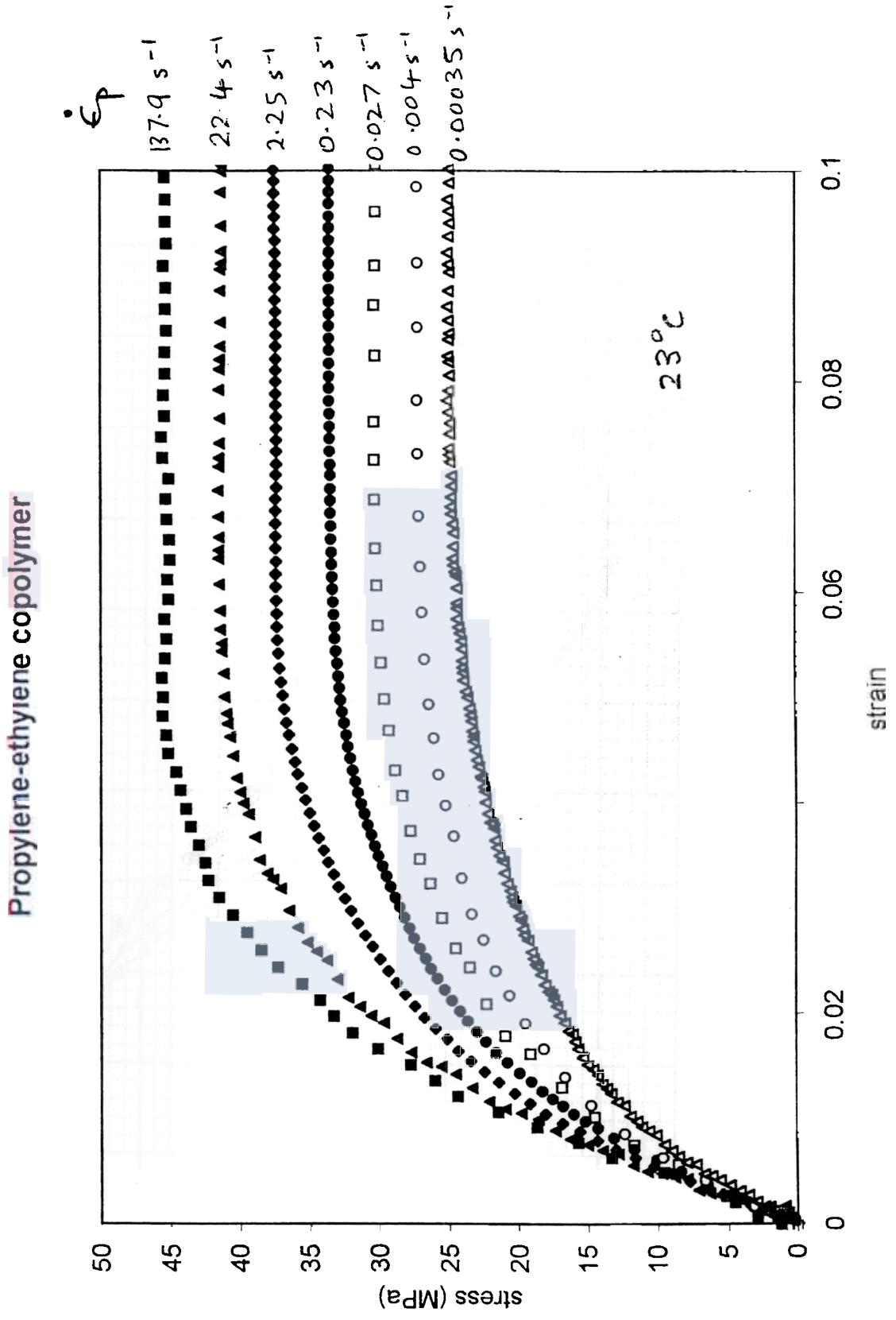


Figure 11 True stress/true strain curves for a propylene copolymer obtained at different strain rates. The rates indicated are for the plastic strain component.

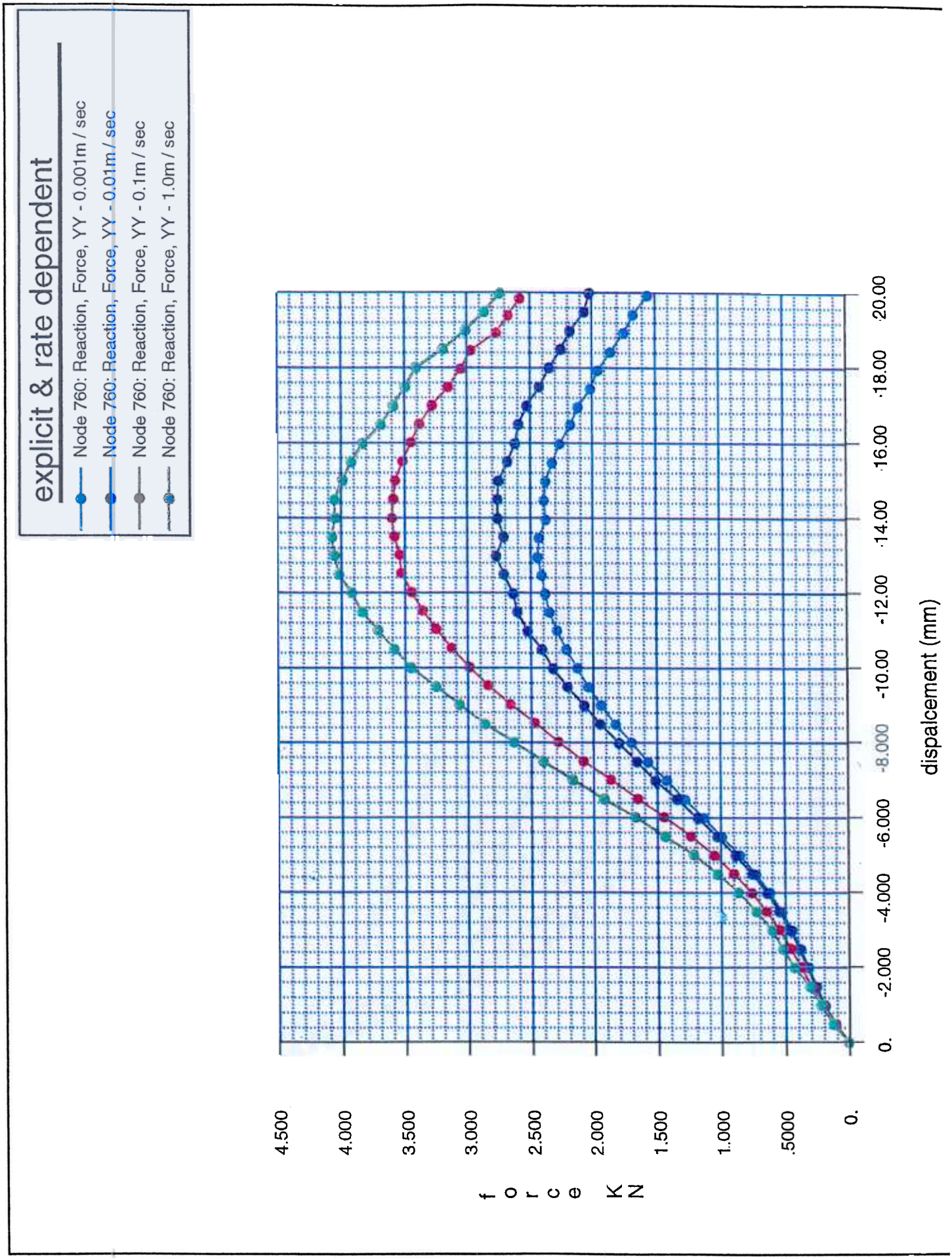


Figure 12 Force/deflection curves calculated for a range of loading speeds using the rate-dependent material properties shown in figure 11.

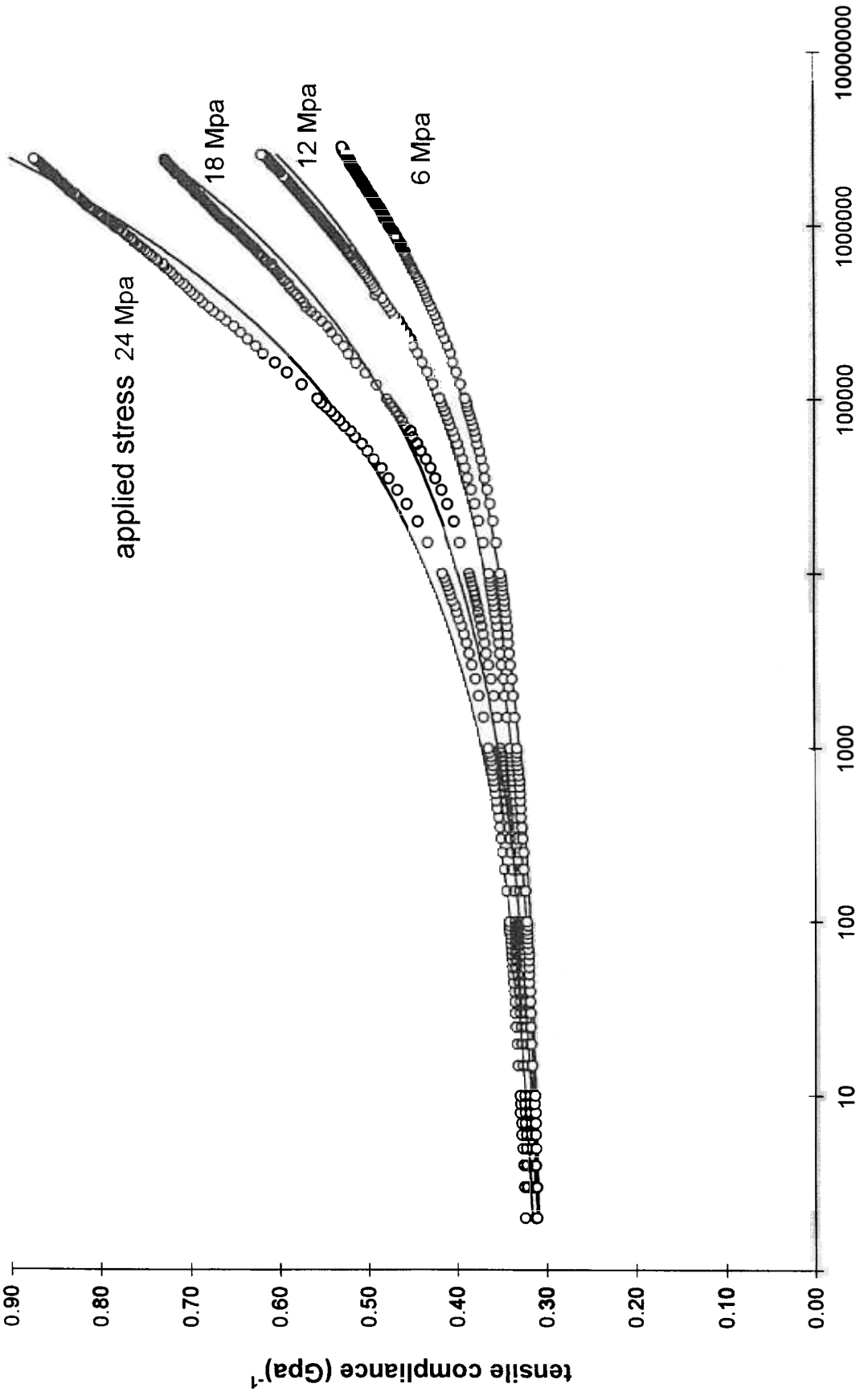


Figure 13 Tensile creep compliance curves for PVC at different levels of applied stress. Creep behaviour is modelled using equations (A12) and (A13) in which the effects of physical ageing have been neglected.

Figure 14 be included at later date

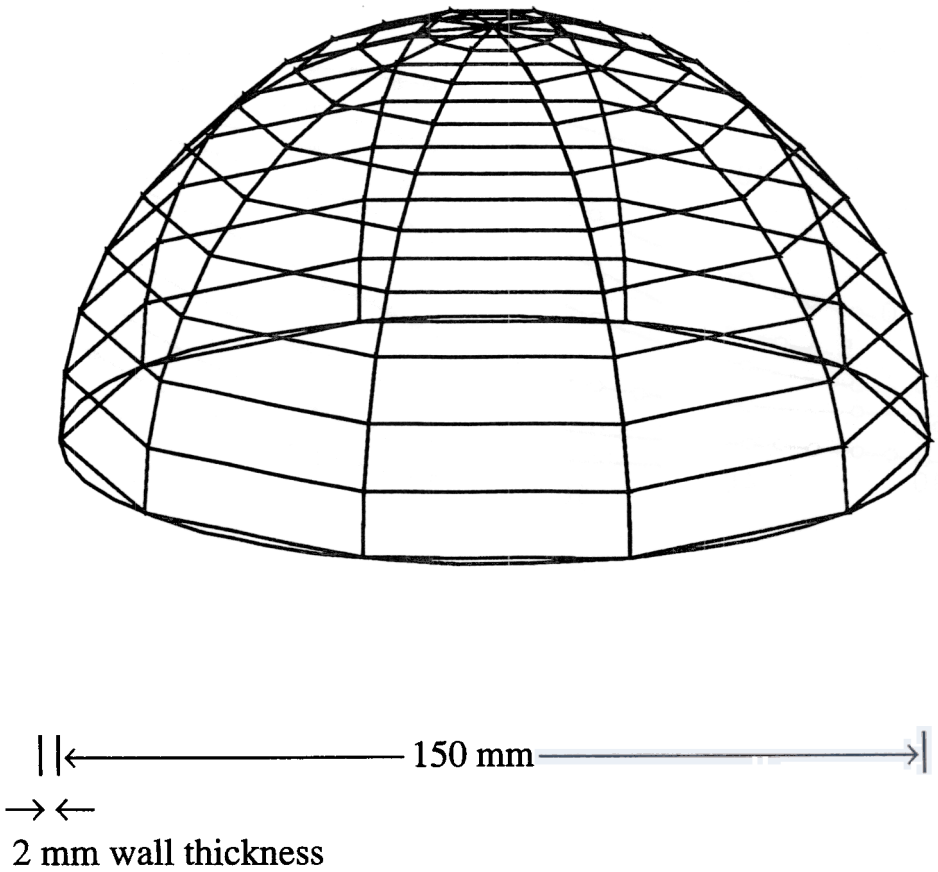


Figure 15 Finite element mesh and dimensions used for the calculation of resonance frequencies of a hemispherical shell of a viscoelastic material

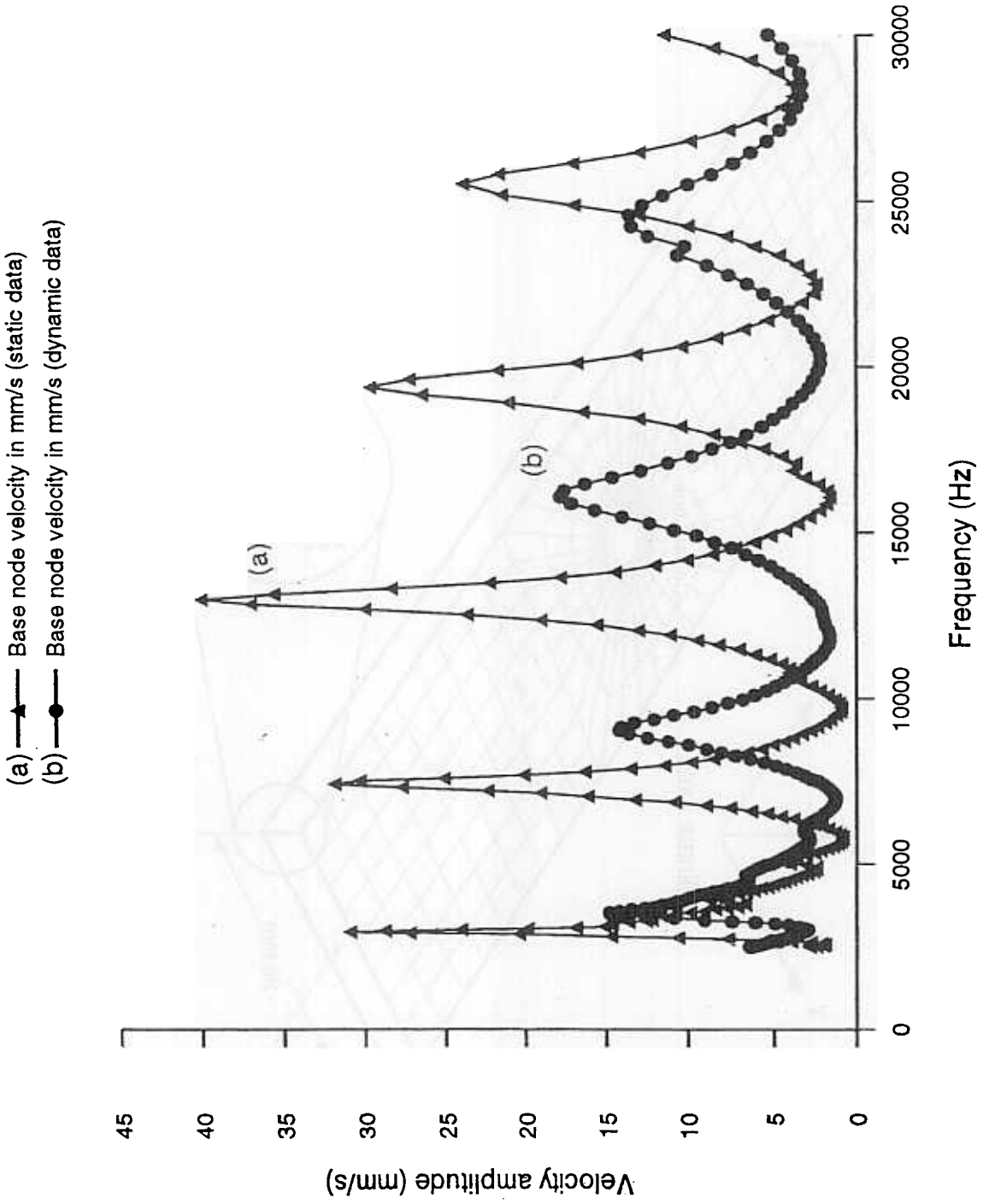


Figure 17 Velocity amplitudes and frequencies of the resonant modes of the hemispherical shell shown in figure 15. Curve (a) was obtained using dynamic property data from figure 16 at a single frequency of 10 Hz. Curve (b) was obtained using data over the whole frequency range.

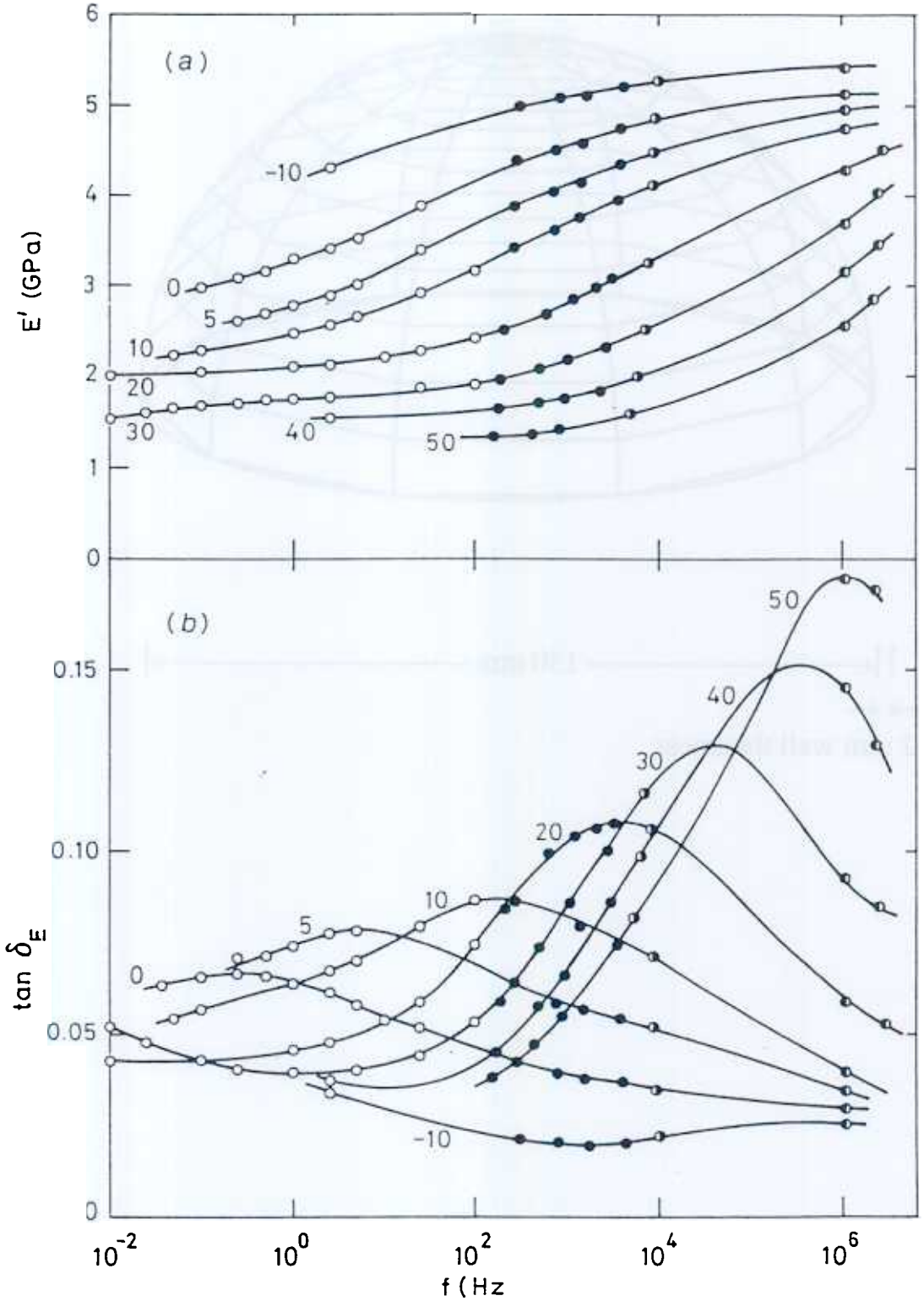


Figure 16 Frequency dependence of (*a*) E' and (*b*) tan δ_E for poly(propylene) at temperatures (°C) indicated on each curve. Symbols are ○, tensile nonresonance method; ●, flexural resonance; ◑, longitudinal resonance; and ◐, ultrasonic pulse technique.

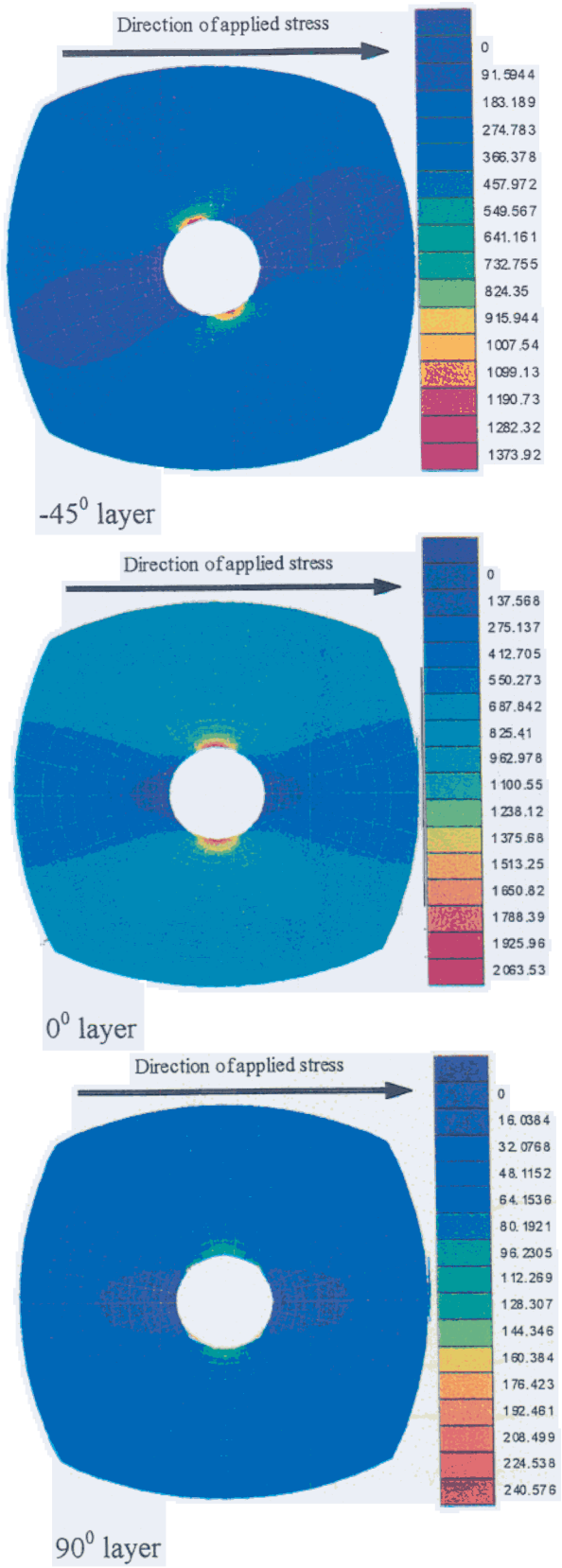


Figure 19 Contours of maximum principle stress (MPa) in each layer produced by a remote stress on the laminate of 140 MPa.

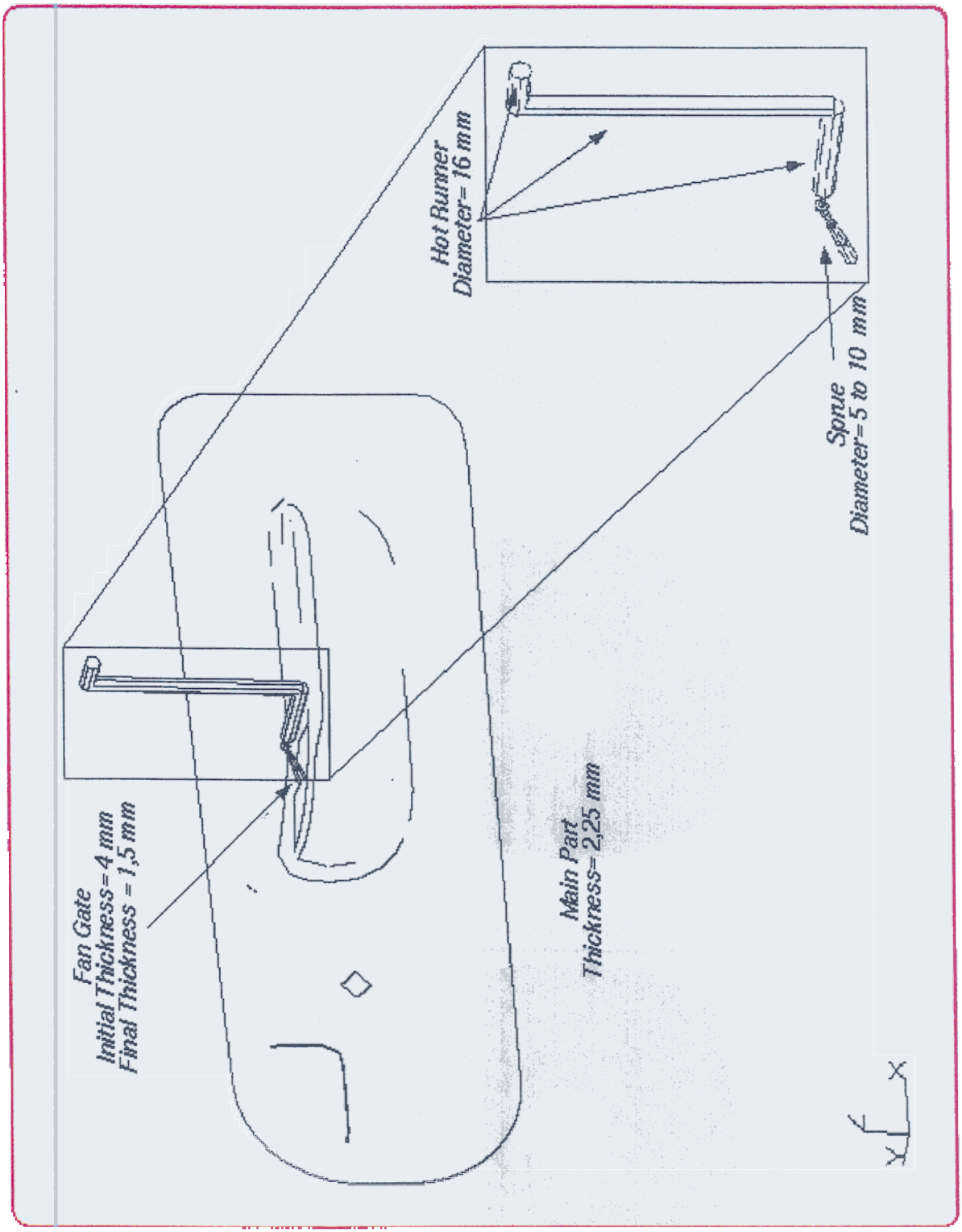


Figure B-1 Automotive door panel geometry and runner system

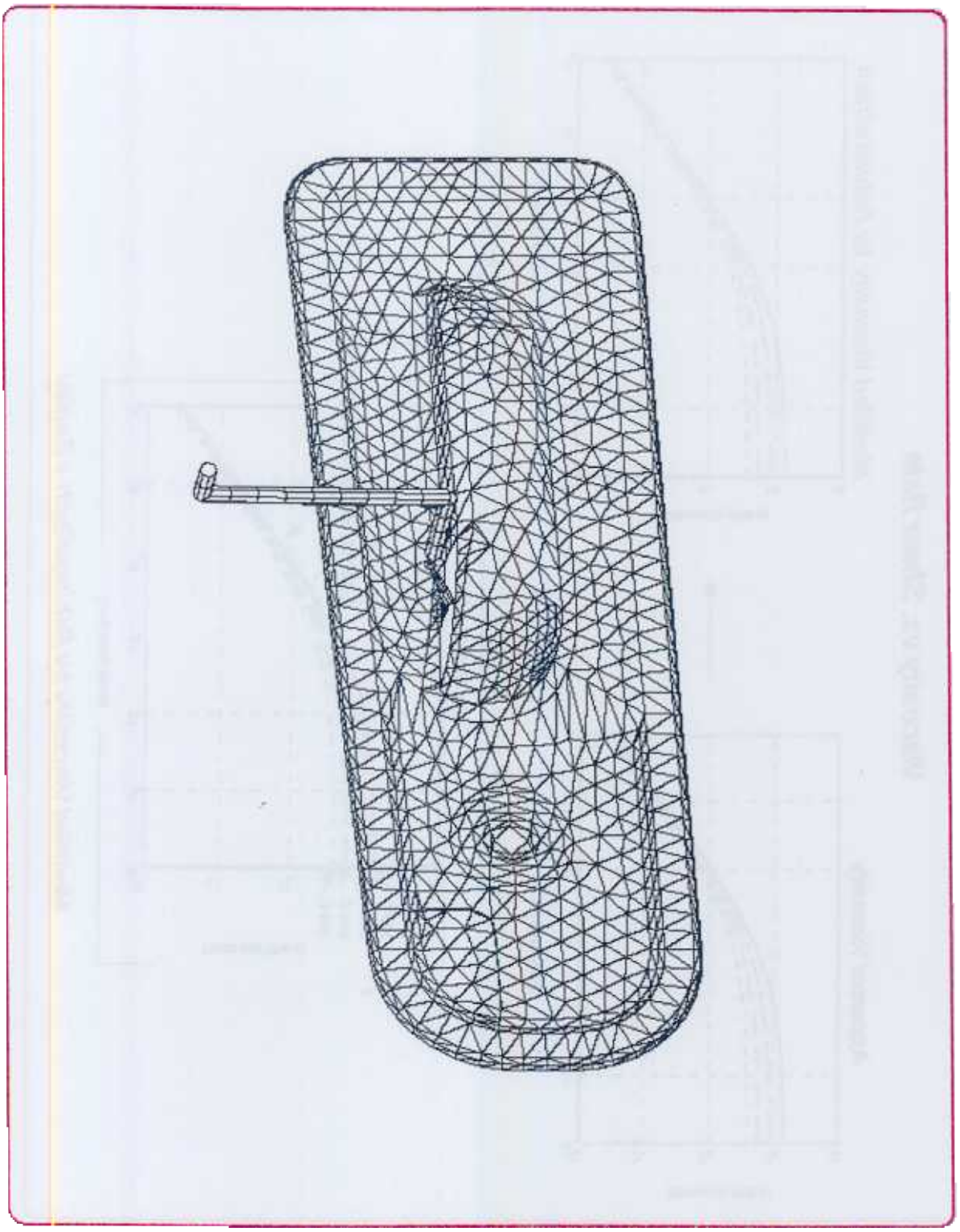


Figure B-2 Finite element mesh used for the simple injection molding simulation of the automotive door panel

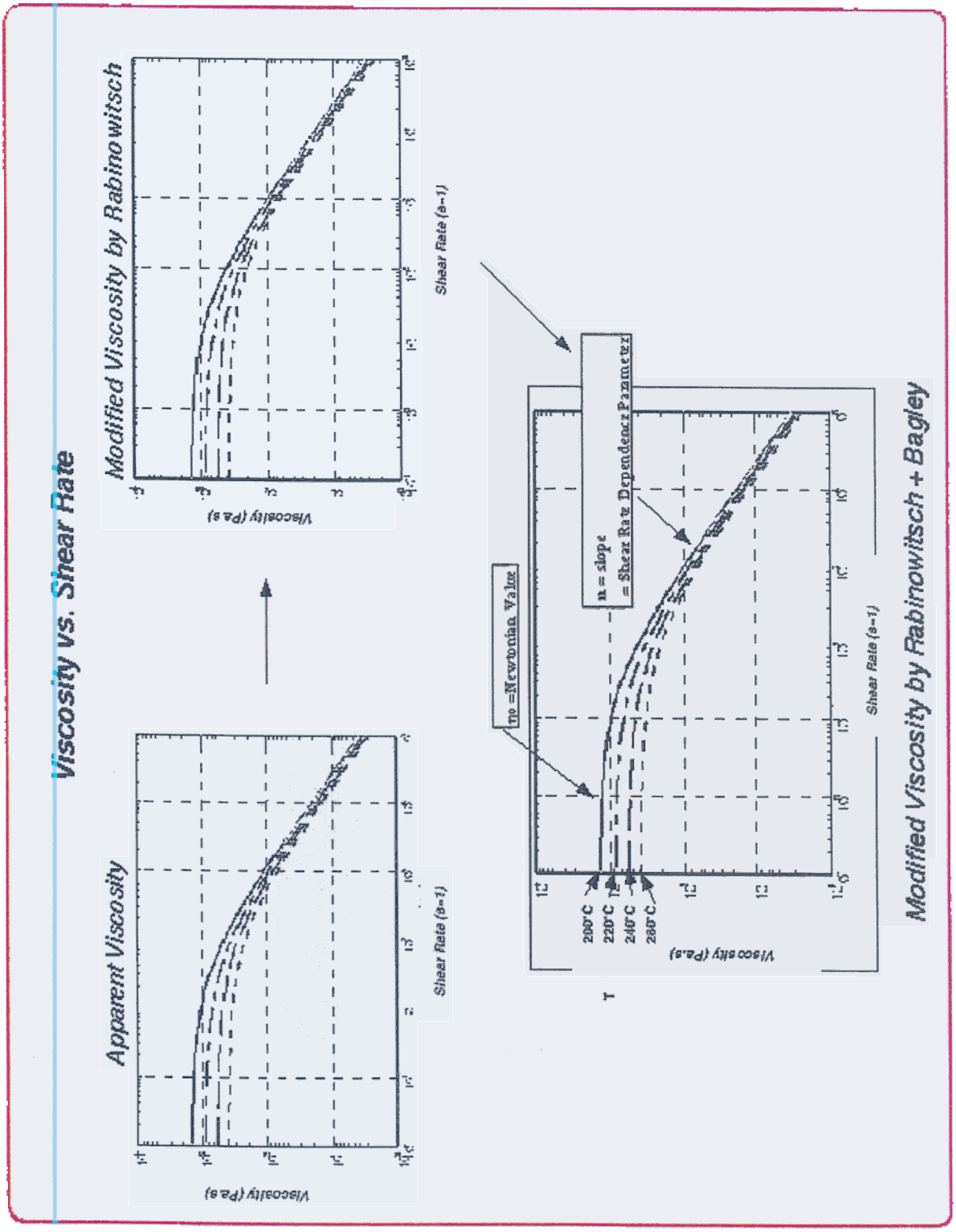
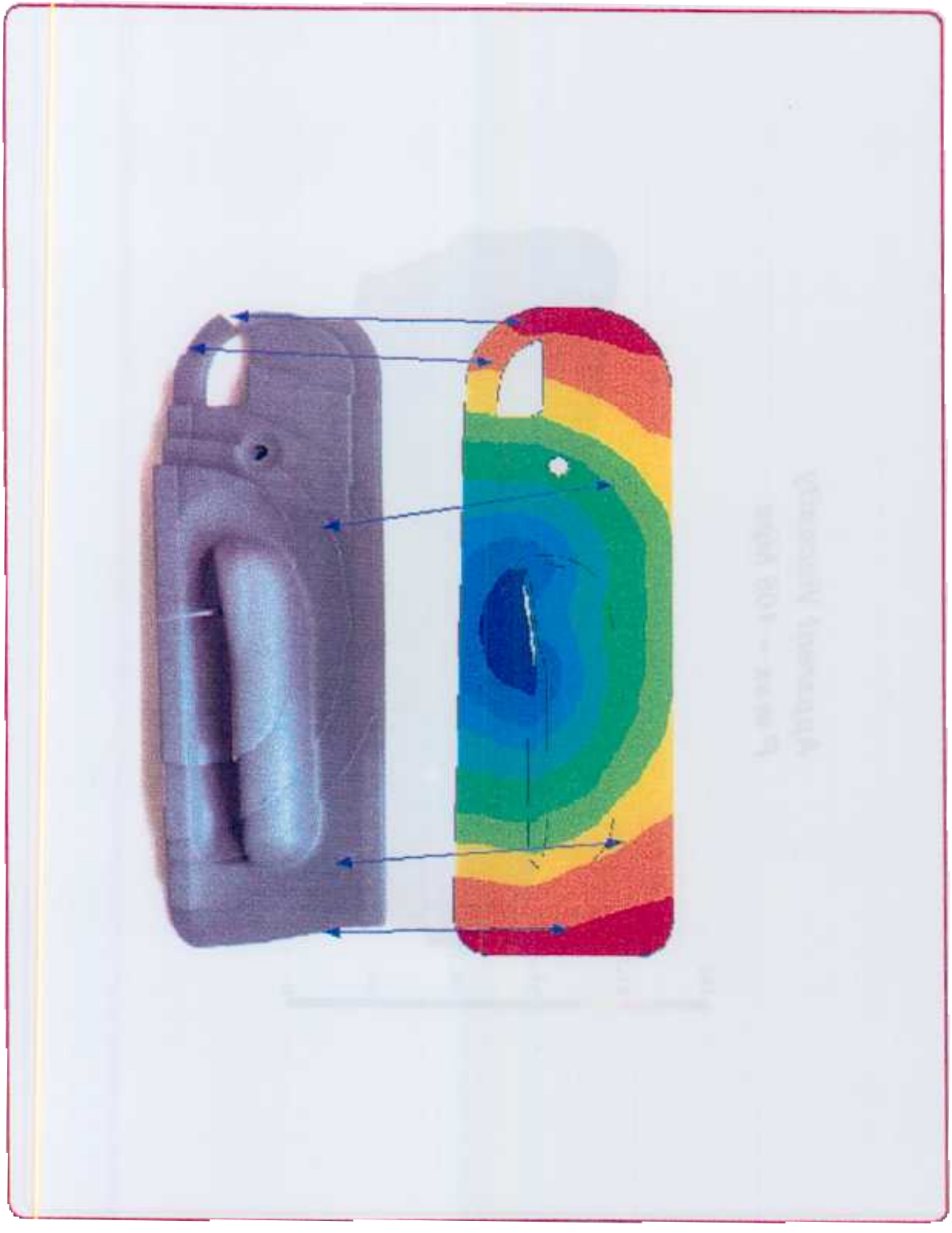


Figure B-3 Representation of Viscosity vs. shear rate data at different temperatures for the three cases



qure B-4 Comparison of the experimental short shots and the numerical simulation melt front advancement

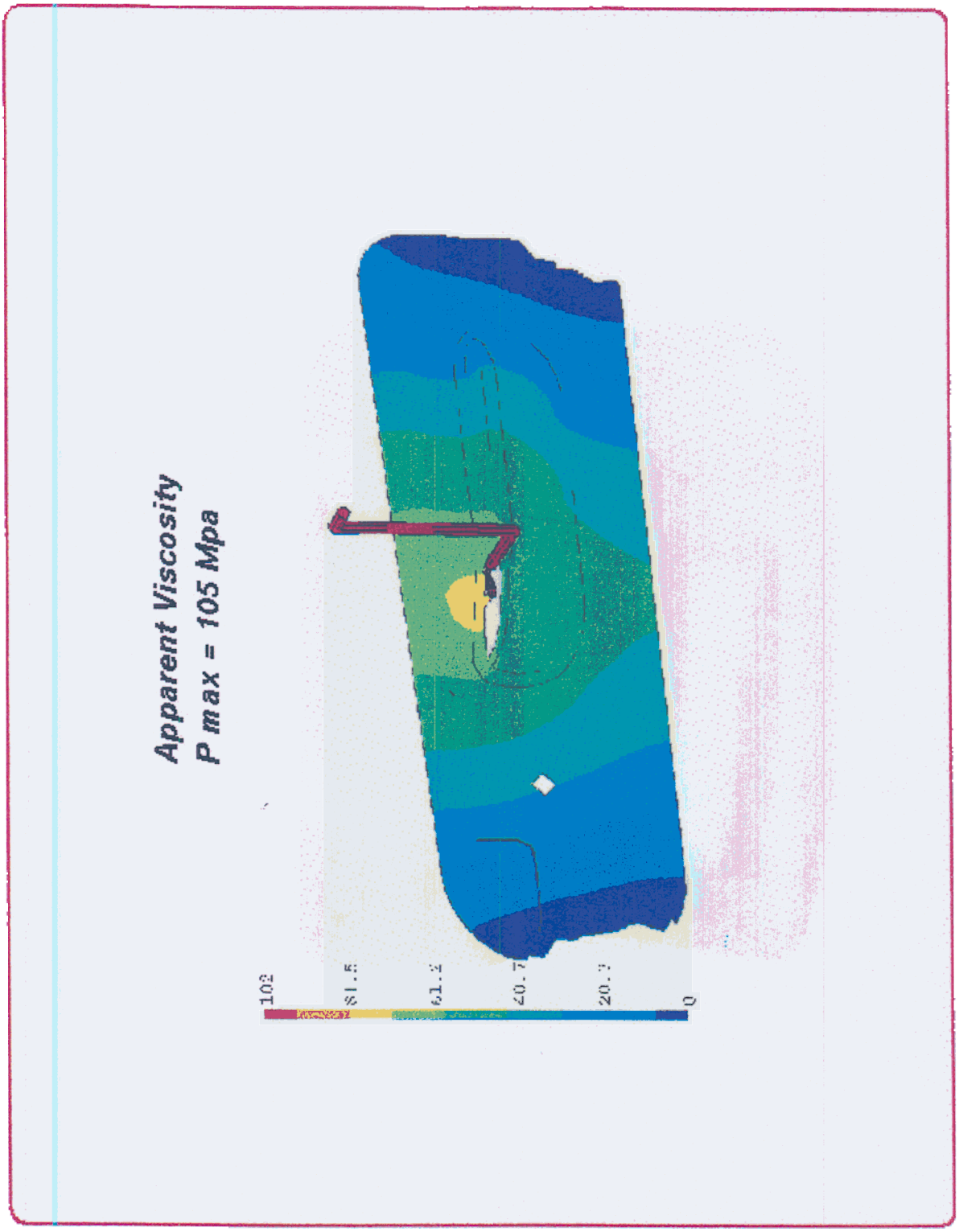


Figure B-5 Pressure distribution at the end of filling stage for case i (using the apparent viscosity)

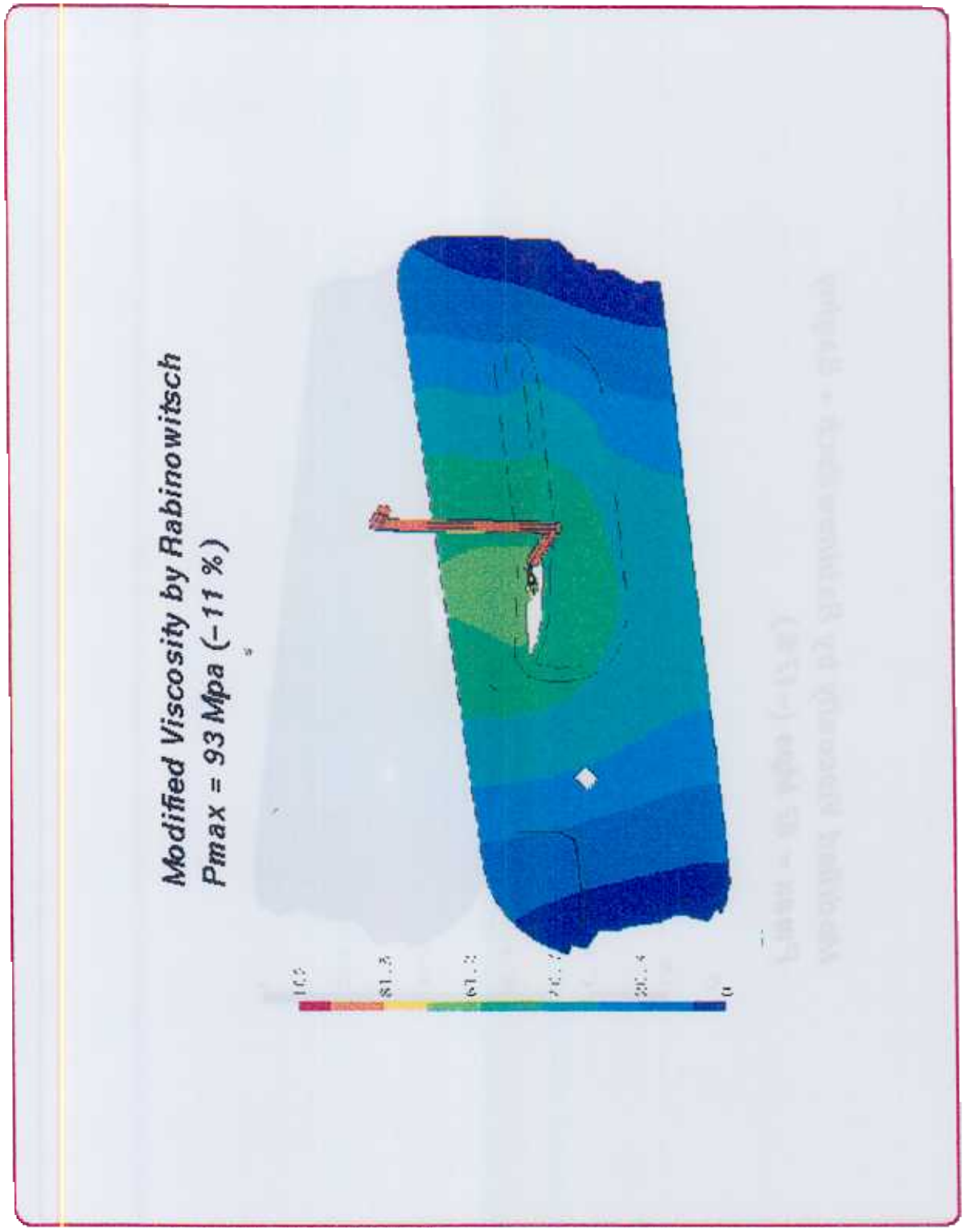


Figure B-6 Pressure distribution at the end of filling stage for case ii (using the modified viscosity with Rabinowitsch correction only)

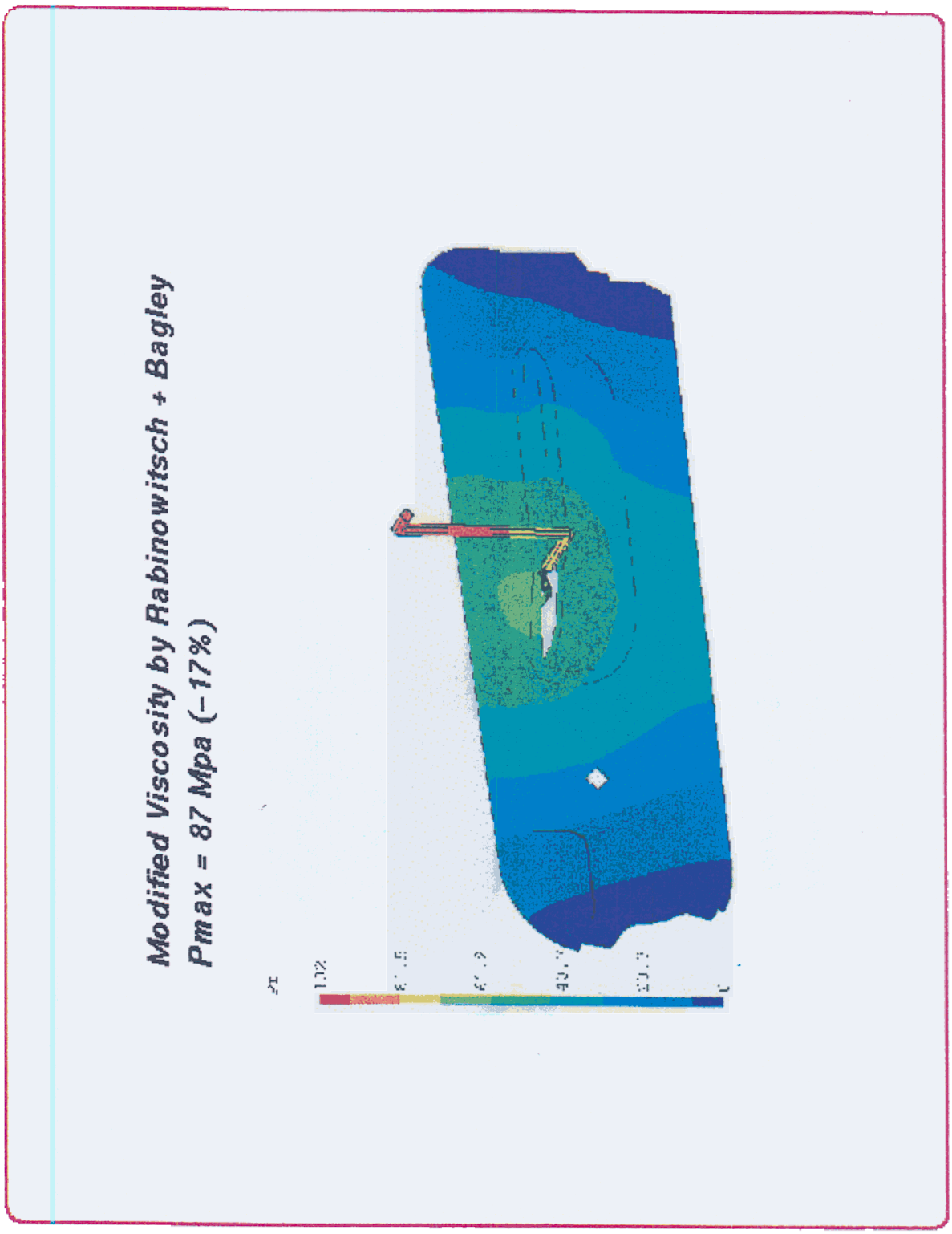


Figure B-7 Pressure distribution at the end of filling stage for case iii (using the modified viscosity with Rabinowitsch and Bagley corrections)

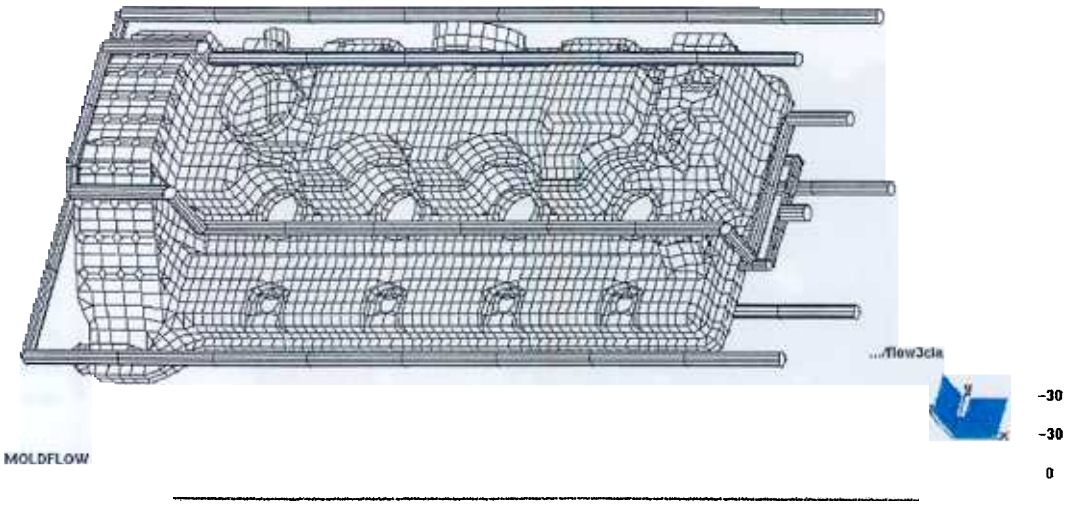


Figure B-8 Model of the rocker cover illustrating the finite element mesh and cooling lines

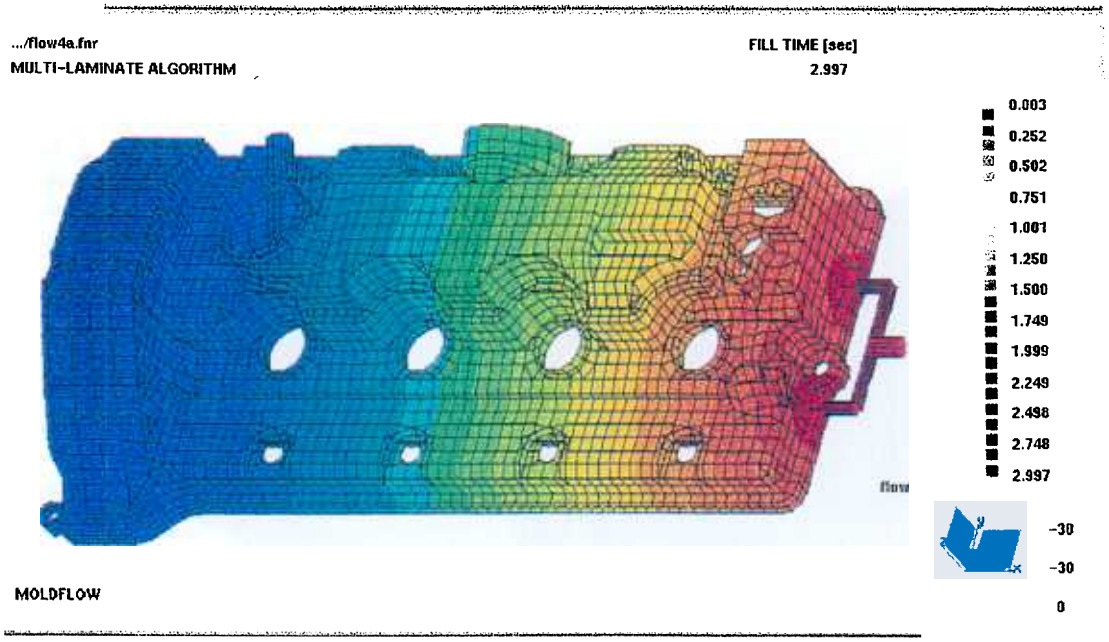


Figure B-9 Computed melt front position versus time for the rocker cover

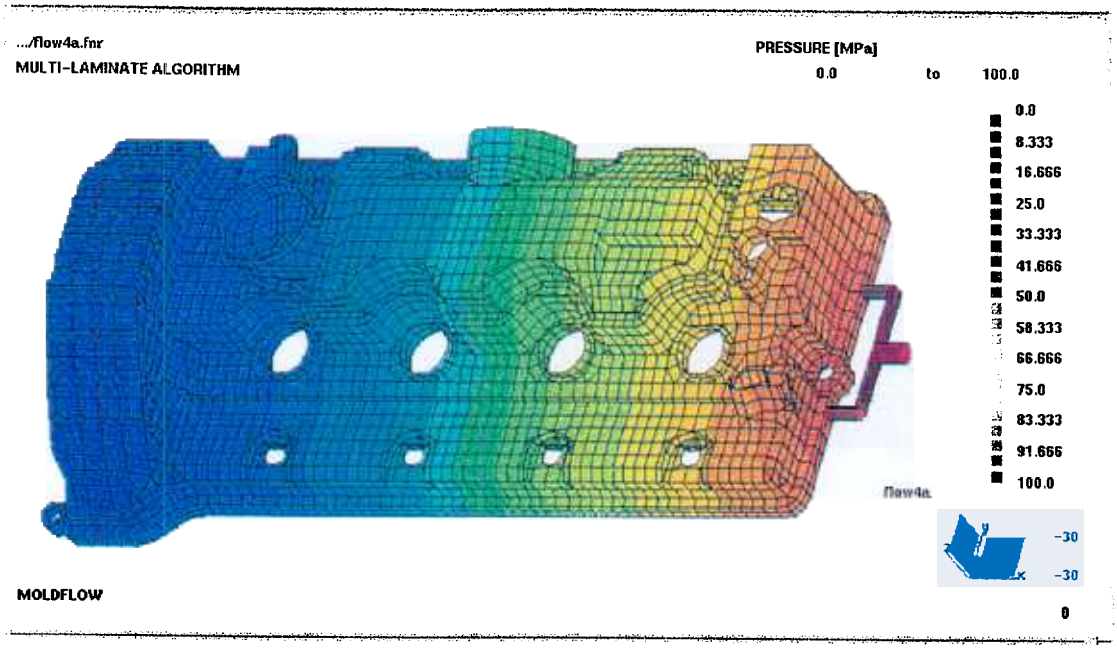


Figure B-10 Pressure distribution at end of filling (i.e. start of packing)

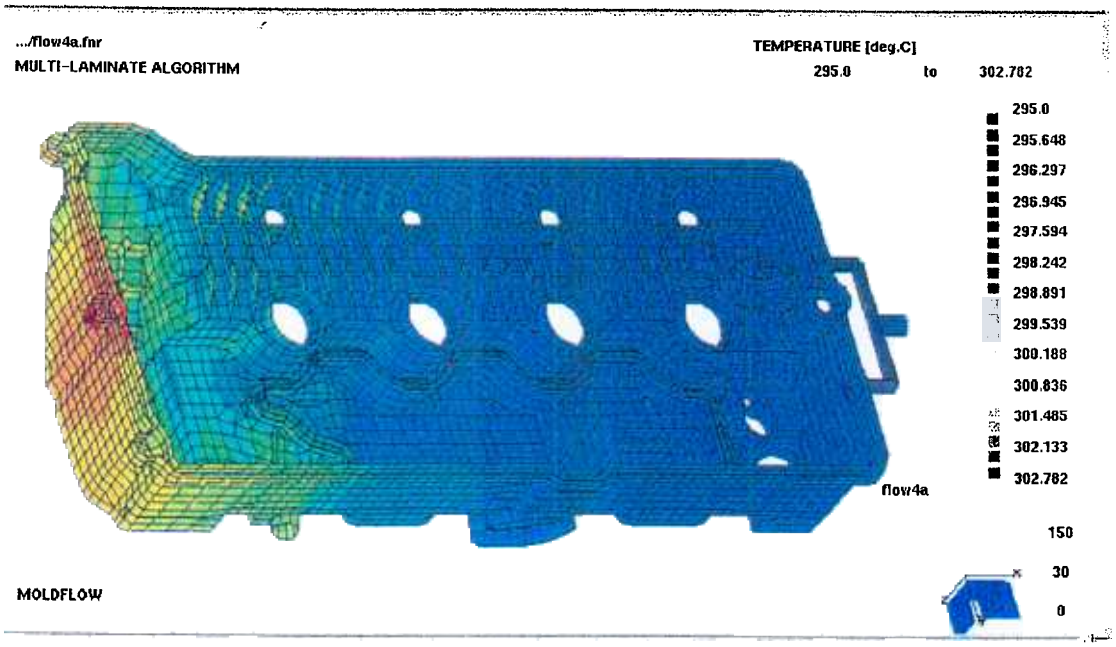


Figure B-11 Computed temperatures for the melt flow-front, when passing through the cover

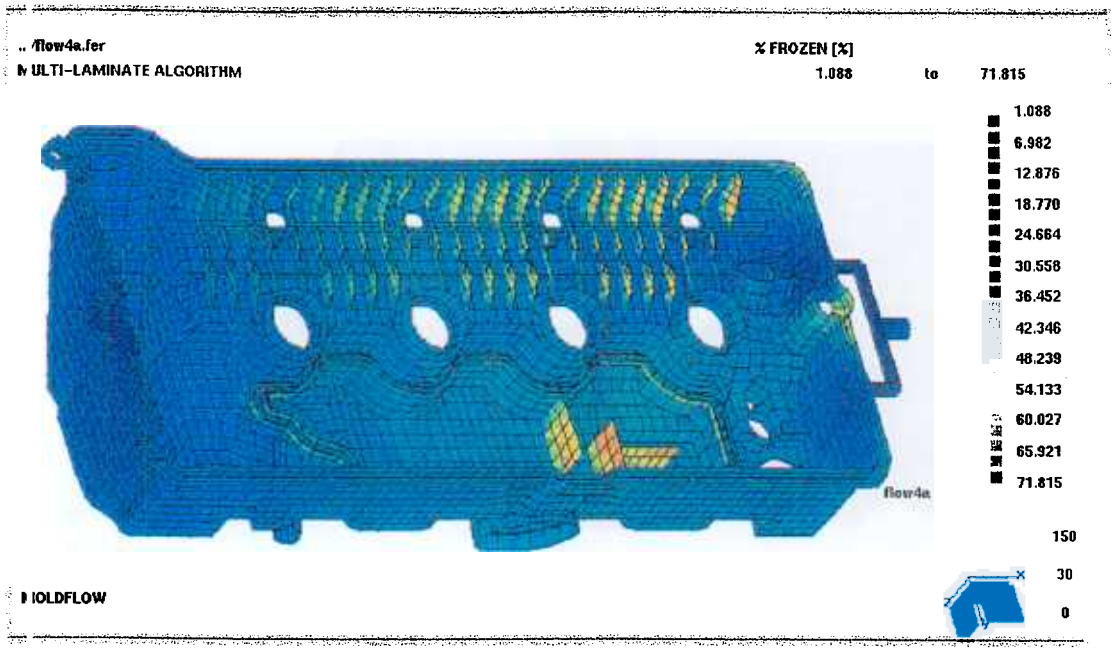


Figure B-12 Computed frozen layer thickness (%) at end of filling

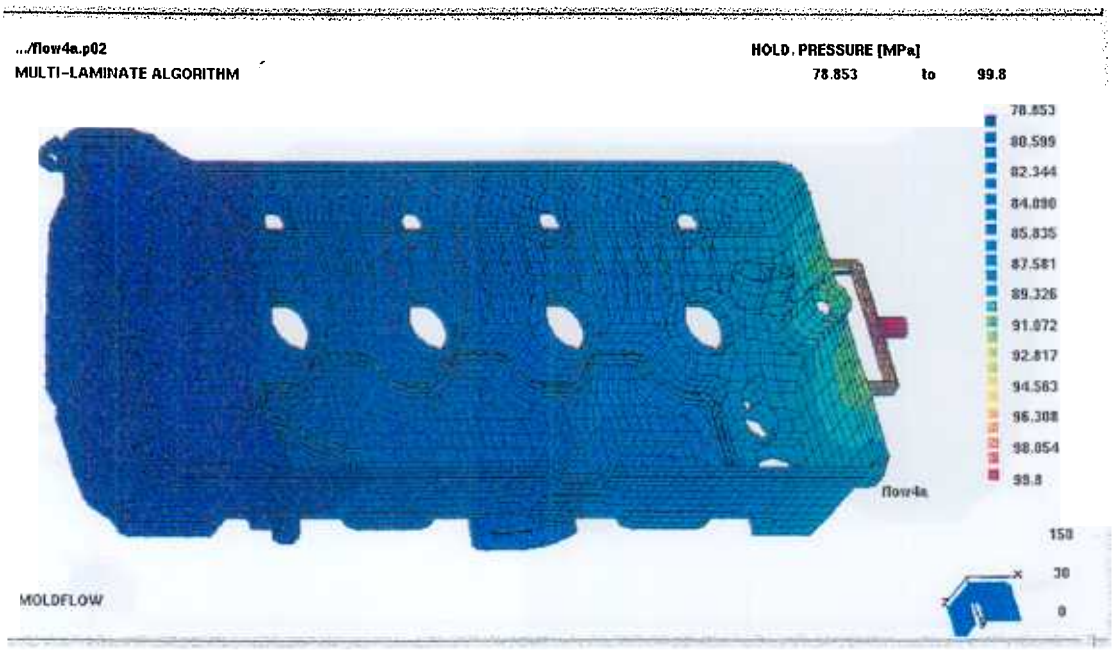


Figure B-13 Computed (maximum) pressure during packing

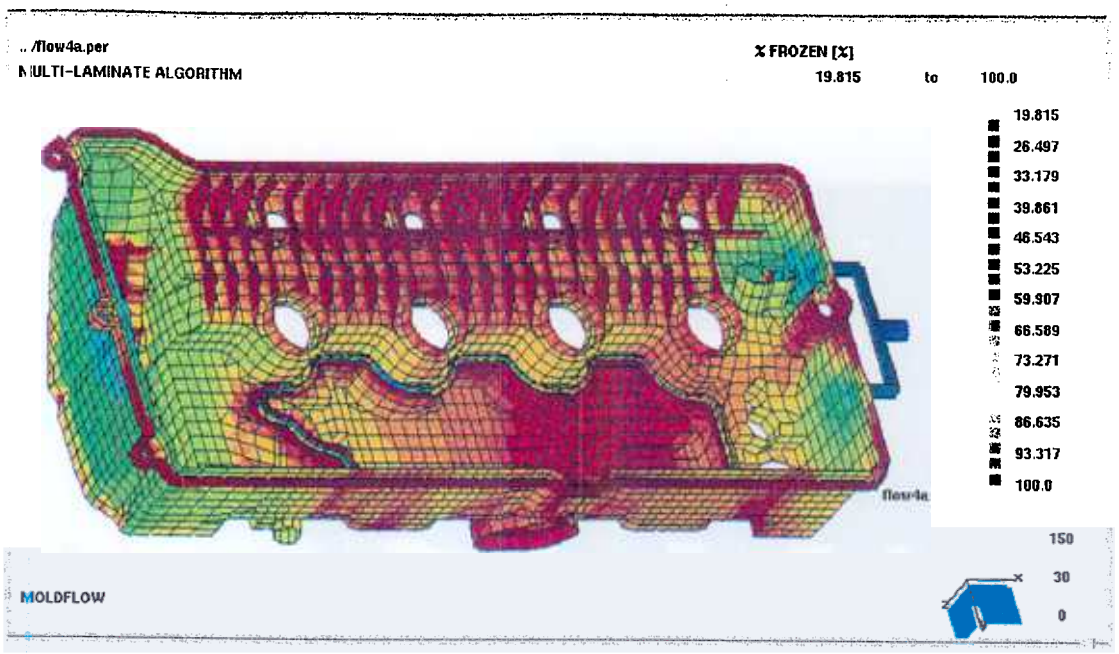


Figure B-14 Computed frozen layer thickness at end of (5 s) packing

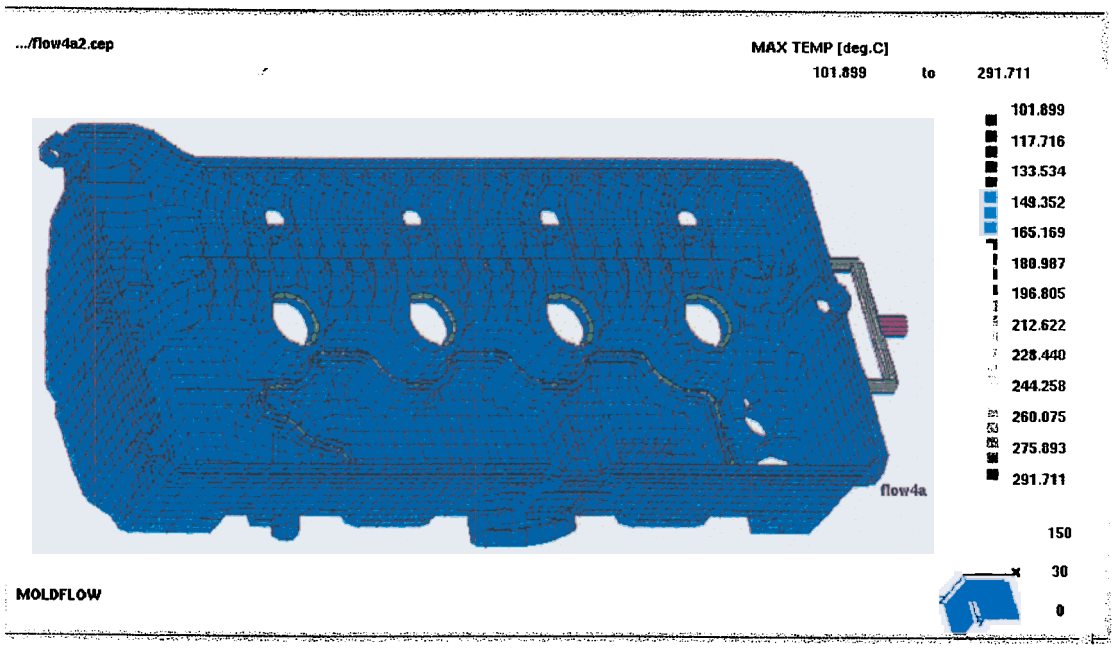


Figure B-15 Computed maximum temperatures over thickness after 25 s cooling

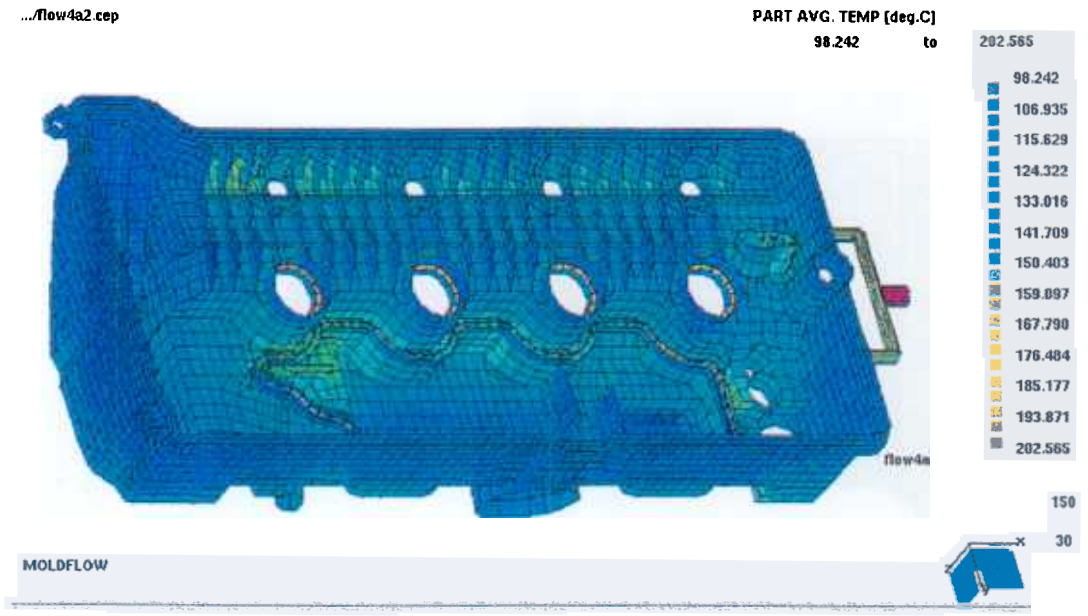


Figure B-16 Computed average temperature over thickness after 25 s cooling

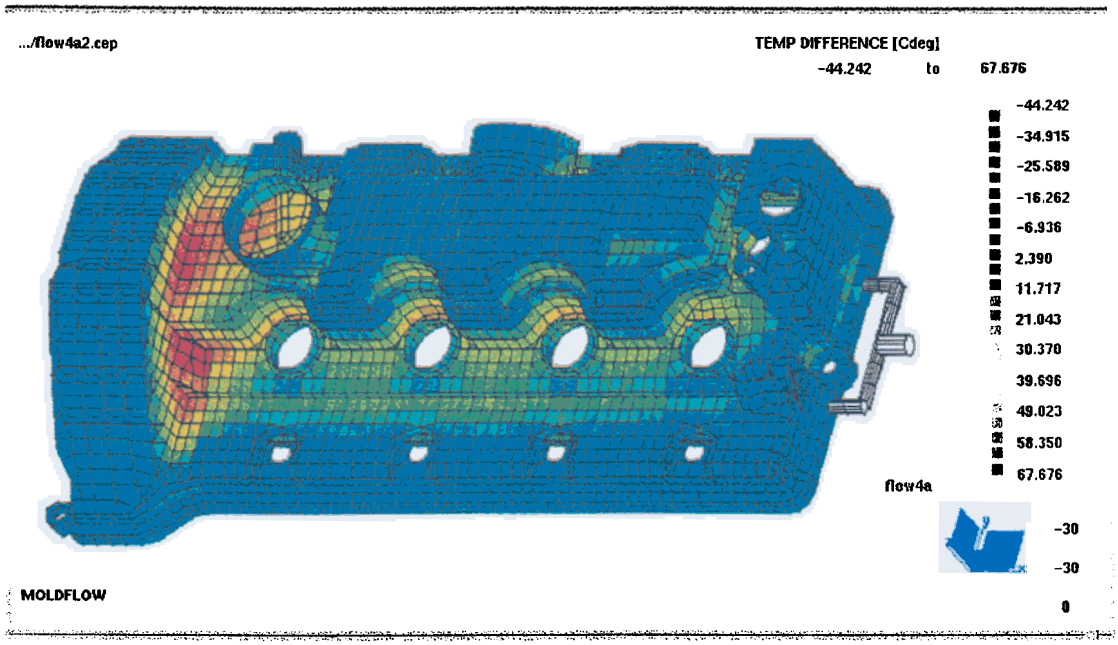


Figure B-17 Computed temperature difference (top-bottom) after 25 s cooling

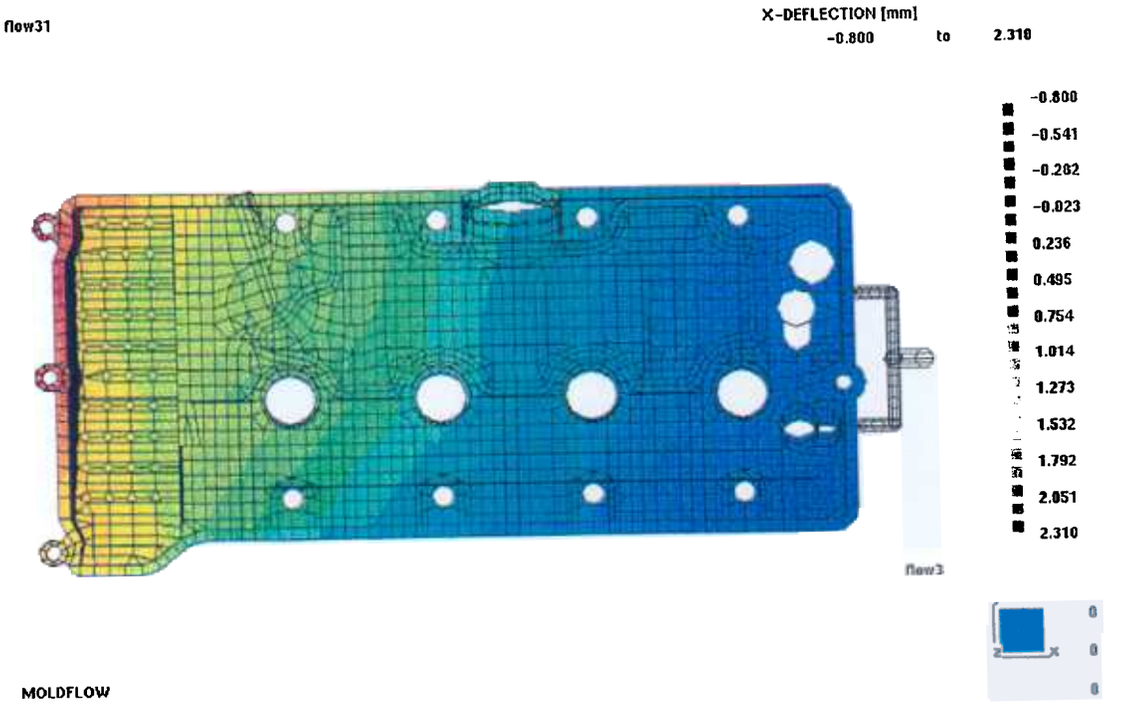


Figure B-18 Computed deformations in X-direction for the rocker cover

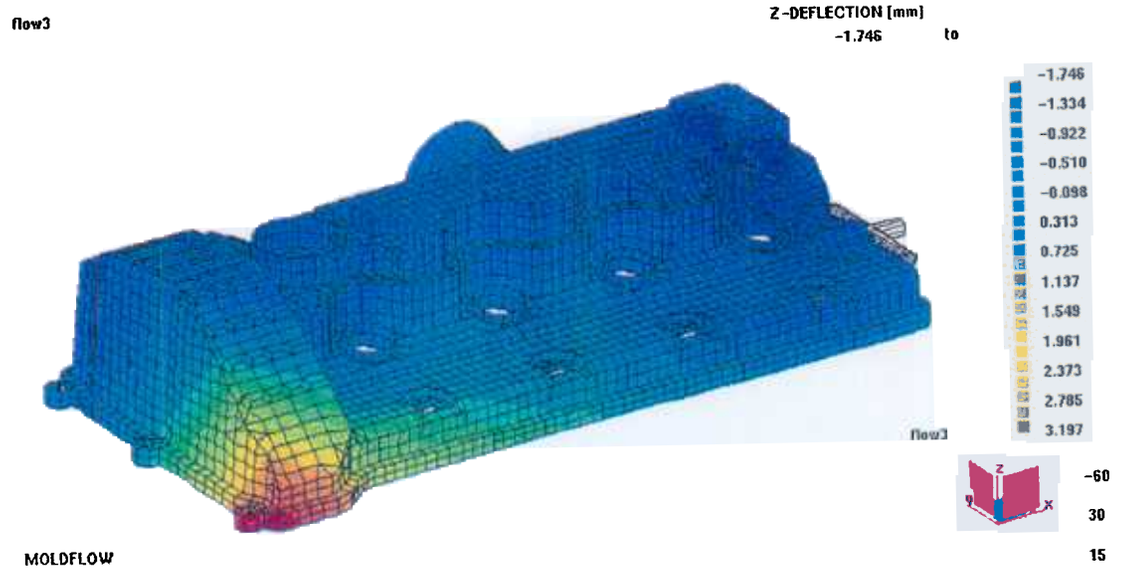


Figure B-19 Computed deformations in Z-direction (warpage) for the rocker cover

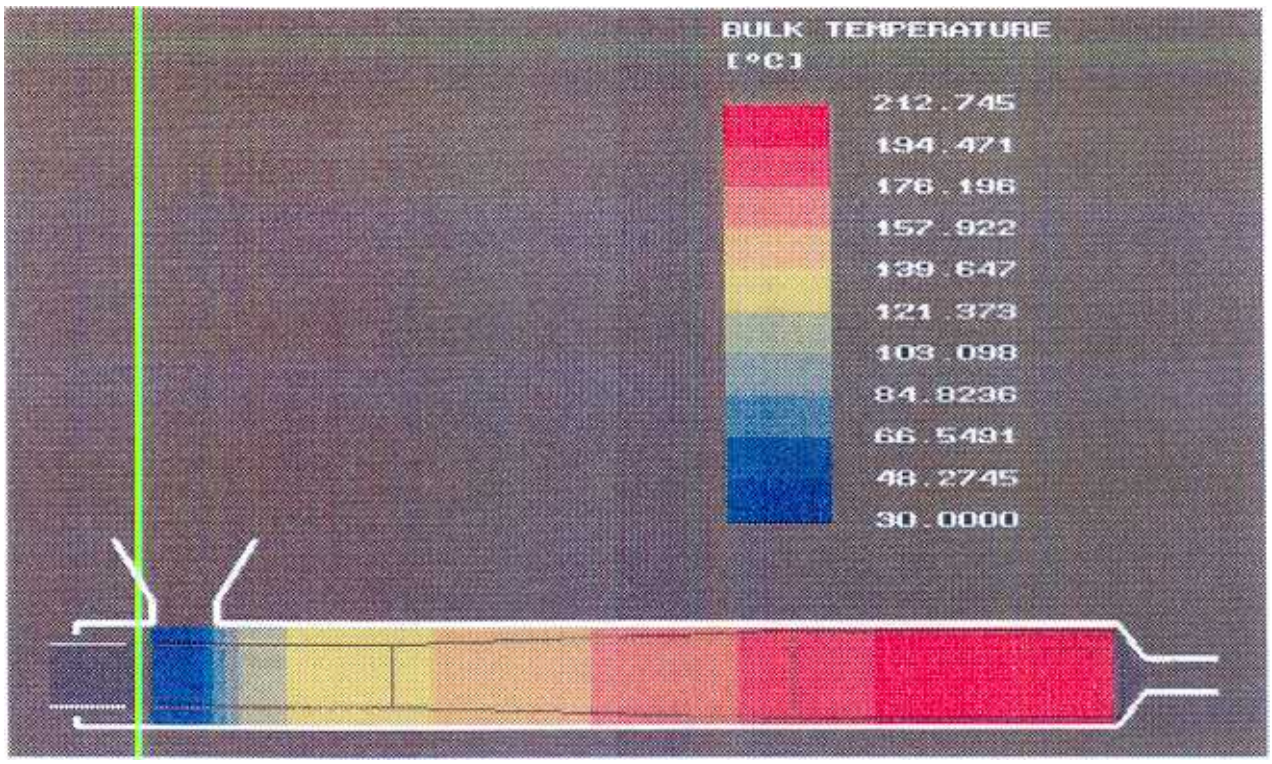


Figure B-20 Computed bulk temperature distribution along the screw length

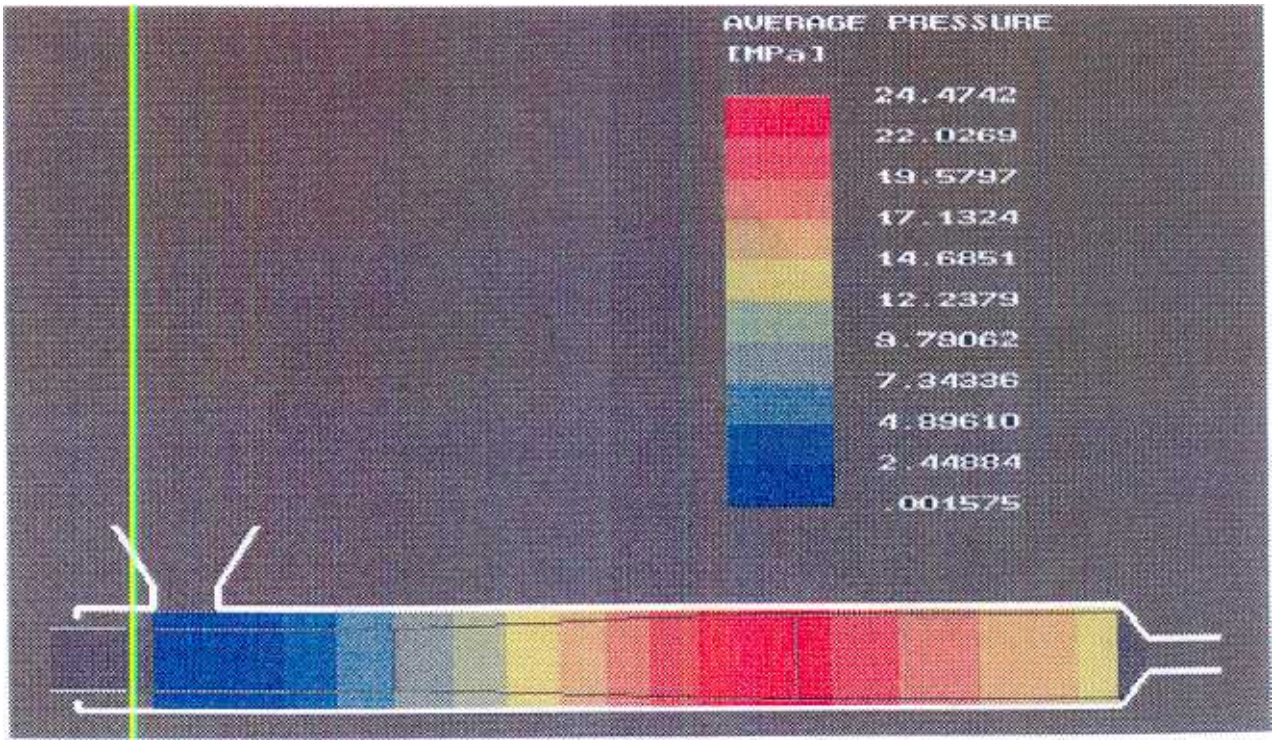


Figure B-21 Computed average pressure distribution along the screw length

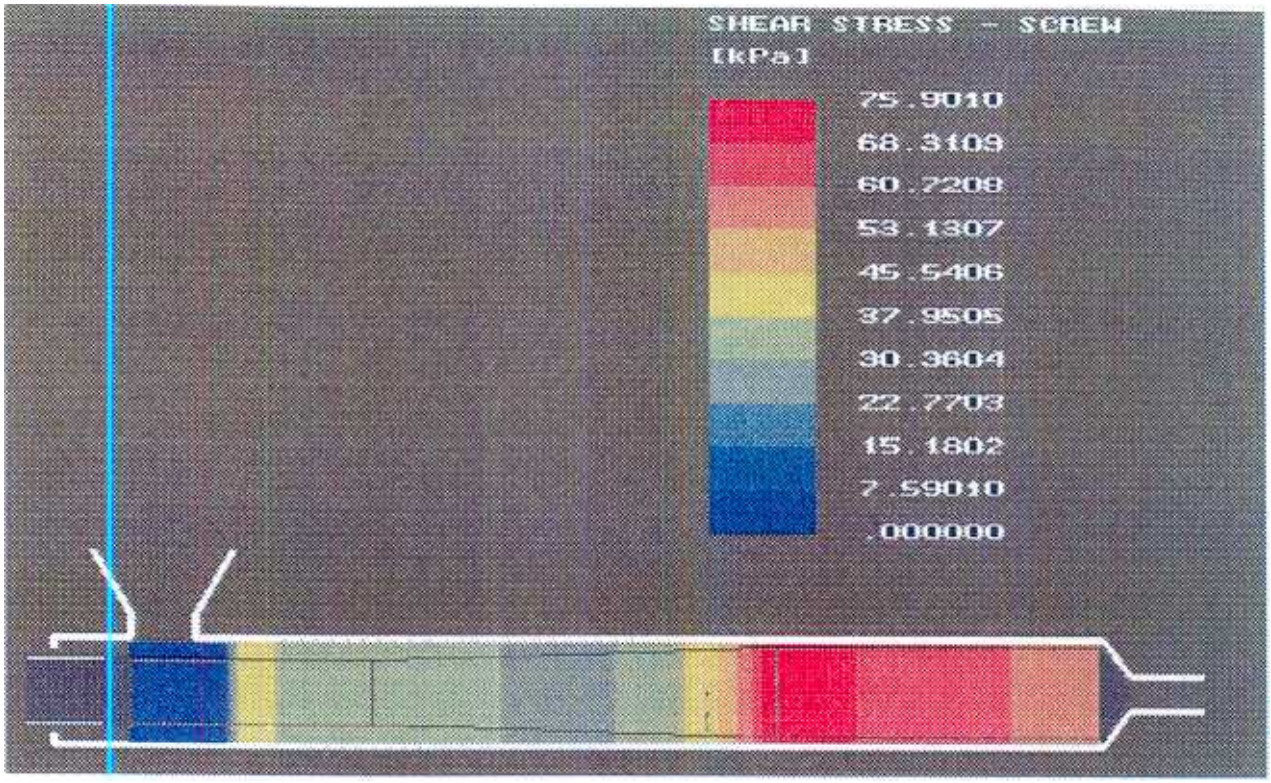


Figure B-22 Computed distribution of shear stress at the screw surface along the screw length

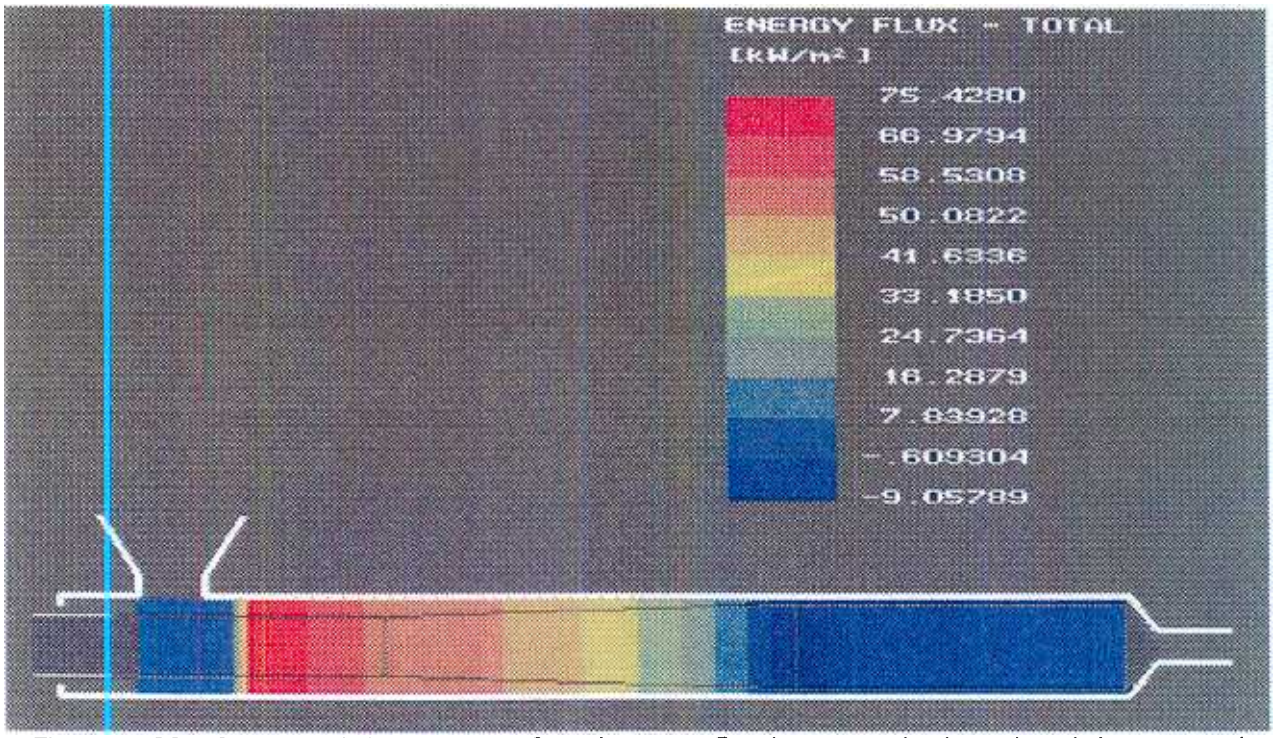


Figure B-23 Computed distribution of total energy flux between the barrel and the material along the screw length

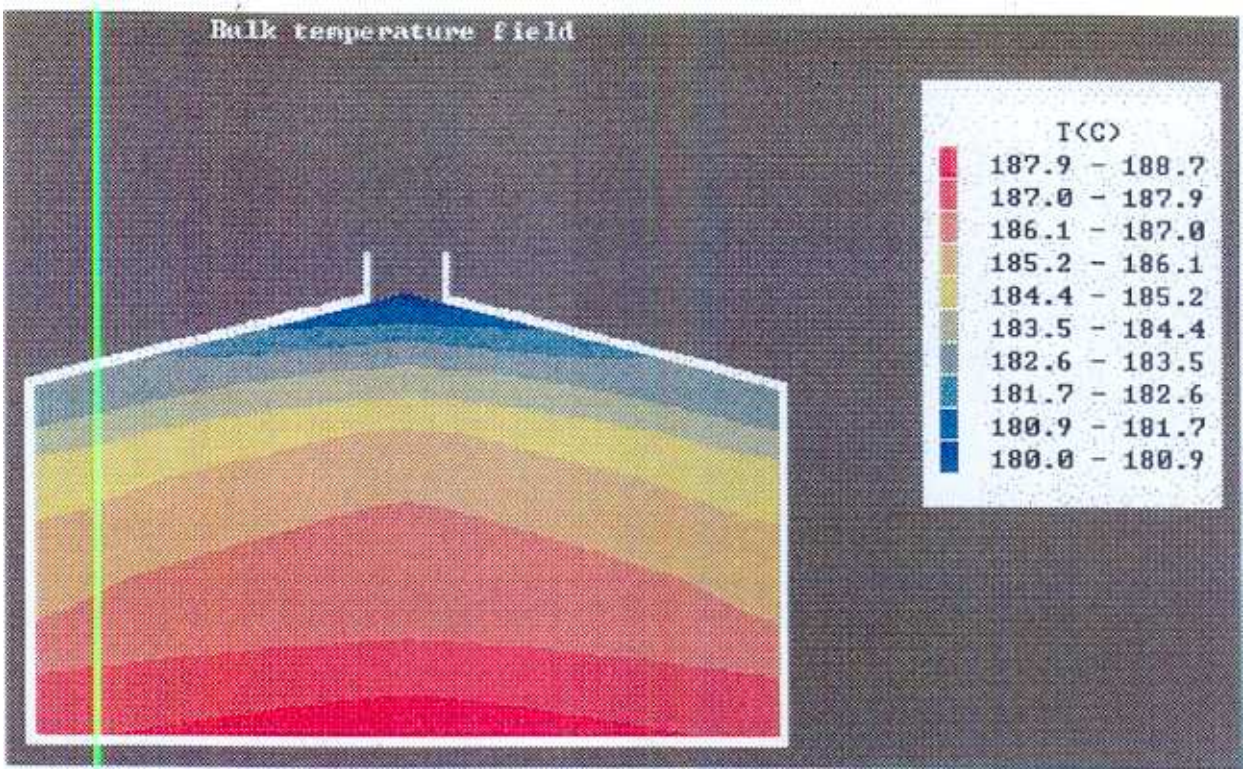


Figure B-24 Computed bulk temperature distribution in the coat hanger die

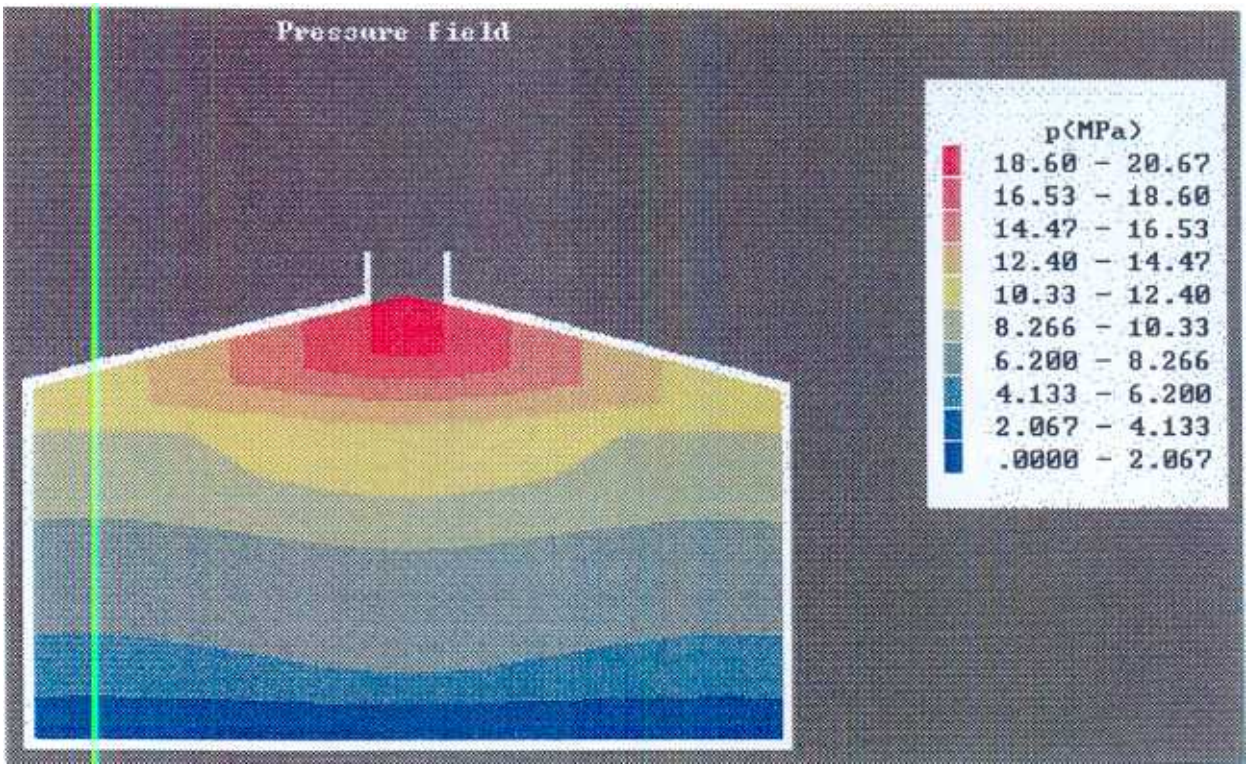


Figure B-25 Computed pressure distribution in the coat hanger die

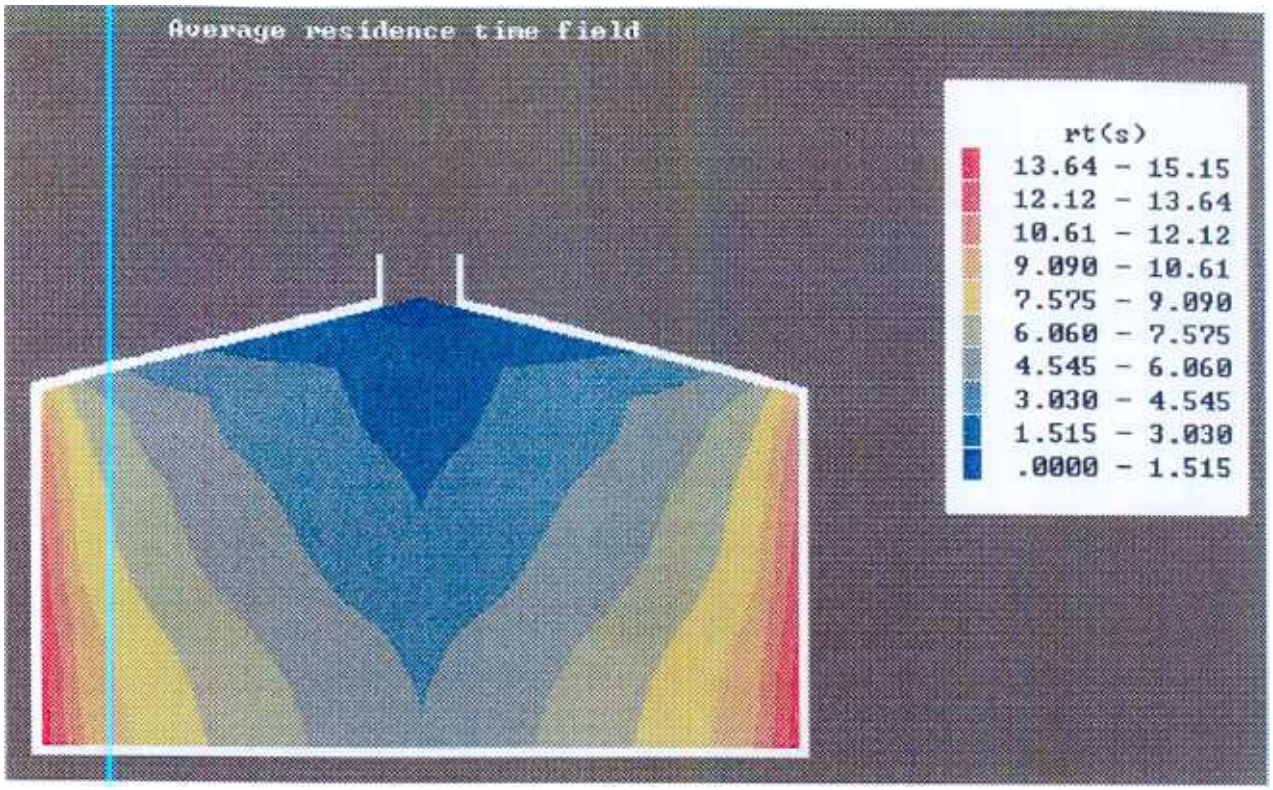


Figure B-26 Computed average residence time distribution in the coat hanger die

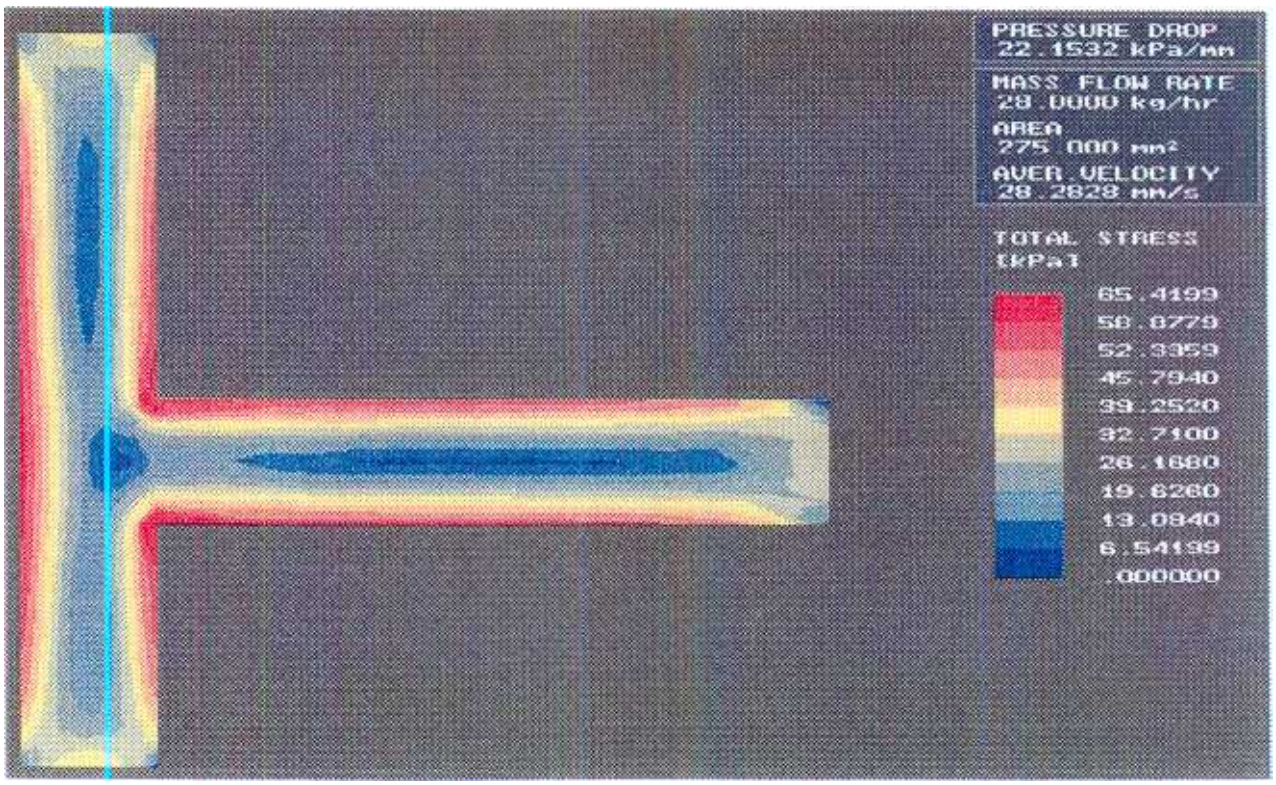


Figure B-27 Computed total stress distribution in the profile die

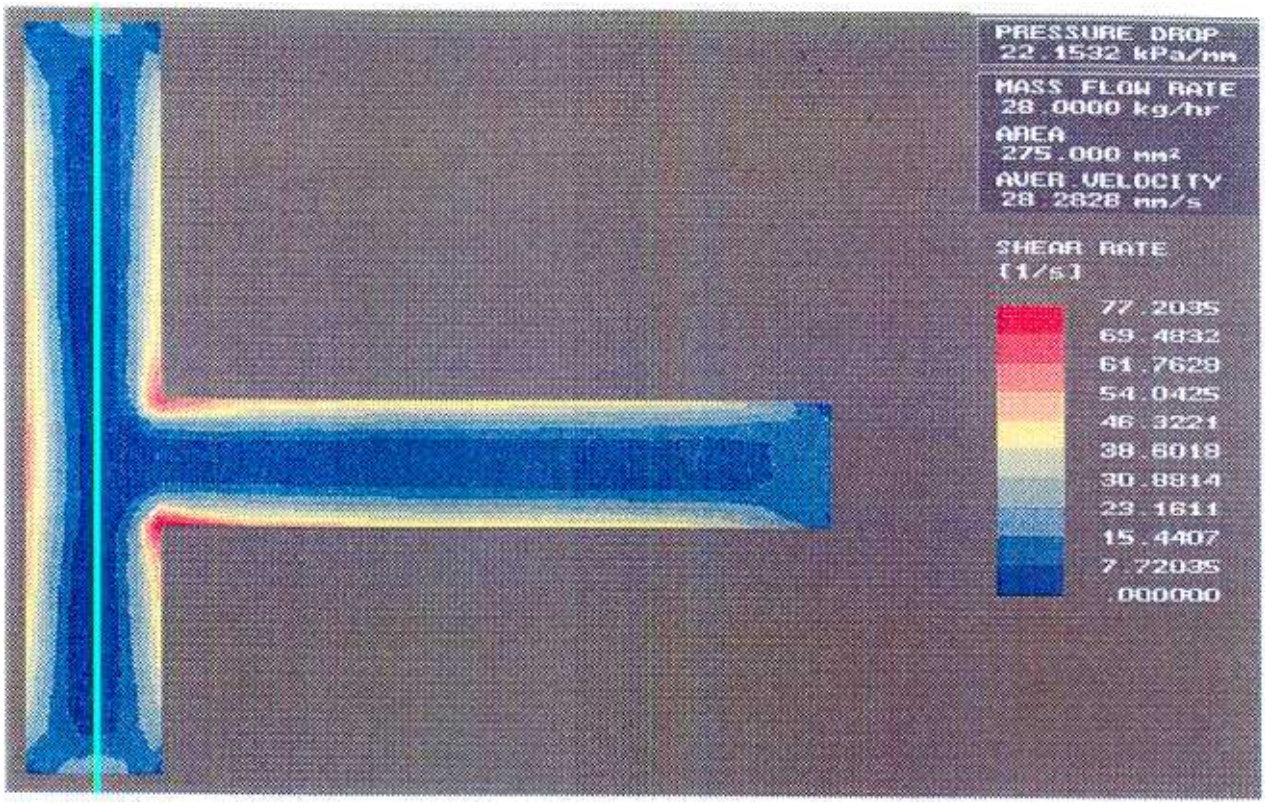


Figure B-28 Computed shear rate distribution in the profile die

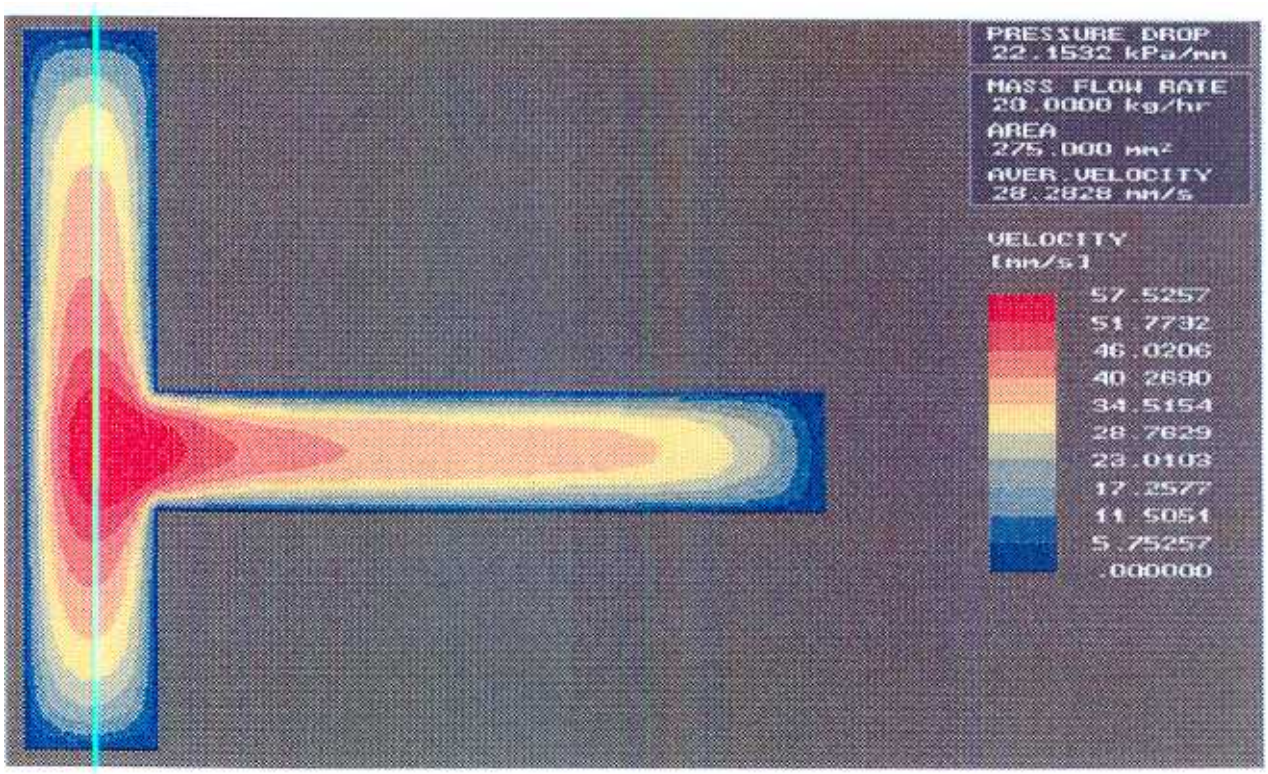


Figure B-29 Computed velocity distribution in the profile die